

# Axisymmetric Deformation of Drops Through Tubes with Asymmetric Constrictions

Submitted to the Graduate School of Natural and Applied Sciences  
in partial fulfillment of the requirements for the degree of

Master of Science

in Mechanical Engineering

by

Büşra Kaya

ORCID 0000-0002-6301-3488

January, 2022

This is to certify that we have read the thesis **Axisymmetric Deformation of Drops Through Tubes with Asymmetric Constrictions** submitted by **Büşra Kaya**, and it has been judged to be successful, in scope and in quality, at the defense exam and accepted by our jury as a MASTER’S THESIS.

**APPROVED BY:**

**Advisor:** **Asst. Prof. Dr. Umut Ceyhan** .....  
İzmir Kâtip Çelebi University

**Committee Members:**

**Assoc. Prof. Dr. Sercan Acarer** .....  
İzmir Kâtip Çelebi University

**Assoc. Prof. Dr. Mehmet Akif Ezan** .....  
Dokuz Eylül University

**Date of Defense: January 27, 2022**

# Declaration of Authorship

I, **Büşra Kaya**, declare that this thesis titled **Axisymmetric Deformation of Drops Through Tubes with Asymmetric Constrictions** and the work presented in it are my own. I confirm that:

- This work was done wholly or mainly while in candidature for the Master's degree at this university.
- Where any part of this thesis has previously been submitted for a degree or any other qualification at this university or any other institution, this has been clearly stated.
- Where I have consulted the published work of others, this is always clearly attributed.
- Where I have quoted from the work of others, the source is always given. This thesis is entirely my own work, with the exception of such quotations.
- I have acknowledged all major sources of assistance.
- Where the thesis is based on work done by myself jointly with others, I have made clear exactly what was done by others and what I have contributed myself.

Signature:

---

Date:

27.01.2022

---

# Axisymmetric Deformation of Drops Through Tubes with Asymmetric Constrictions

## Abstract

Drop deformation in constricted passages plays a vital role in porous media, microfluidic devices etc. Depending on the viscosity ratio, Capillary number, drop volume and geometry of the constriction drops may breakup by the snap-off mechanism. Different from the previous studies that consider symmetric single/periodic constrictions, we model a tube with an asymmetric constriction which is natural in porous media or can be used in microfluidic devices for the control of deformation and/or breakup mechanism. We integrate the drop evolution using the axisymmetric boundary integral equations. Compared with the symmetric constriction, the asymmetry of the constriction affects the snap-off time and thus the volume of the droplet generated after snap-off. The volume is particularly affected by the smoothness of the upstream rather than the downstream of the constriction, delaying the snap-off time as more drop volume moves into to the constriction. We show that in the case of a drop does not snap-off while passing through the constriction an asymmetric design of this passage may lead the snap-off. Pressure drop variation with time across the tube distinguishes the stages of snap-off from escape. To show the importance of the azimuthal curvature on the snap-off mechanism, finally, we compare axisymmetric models with planar flows.

**Keywords:** Snap-off, asymmetric constriction, axisymmetric drop deformation, Stokes flow, boundary integral equations, boundary element method

# Asimetrik Daralmalara Sahip Borularda Damlaların Aksisimetrik Deformasyonu

## ÖZ

Daralan tüp ve borulardaki damla deformasyonu, gözenekli ortamlarda, mikro akışkan cihazlarda vb. önemli bir rol oynar. Damlalar, viskozite oranına, Kapiler sayısına, damla hacmine ve daralma geometrisine bağlı olarak kopma mekanizması ile parçalanabilir. Simetrik tek/periodyk daralmaları dikkate alan önceki çalışmalardan farklı olarak, gözenekli ortamlarda doğal olan veya deformasyon ve/veya parçalanma mekanizmasının kontrolü için mikro akışkan cihazlarda kullanılabilen asimetrik daralmaya sahip bir tüp modelliyoruz. Aksi-simetrik sınır integral denklemlerini kullanarak damlanın gelişimini inceliyoruz. Simetrik daralma ile karşılaştırıldığında, daralmanın asimetrisi, kopma süresini ve dolayısıyla kopmadan sonra oluşan damlacığın hacmini etkilemektedir. Hacim, daralmanın aşağı akış bölgesinden ziyade yukarı akış bölgesinin düzgünlüğünden etkilenmektedir ve daralmaya daha fazla damla hacmi hareket ettikçe kopma süresi gecikmektedir. Daralma içinden geçerken bir damlanın kopmaması durumunda, bu geçidin asimetrik tasarımının kopmaya yol açabileceğini gösteriyoruz. Damlanın koptuğu bir durum ile daralmadan kaçabildiği durumların farkını tüp boyunca basınç düşüşünün zamanla değişimi ile gözlemliyoruz. Son olarak, azimut eğriliğinin kopma mekanizması üzerindeki önemini göstermek için, aksi-simetrik modelleri düzlemsel akışlarla karşılaştırıyoruz.

**Anahtar Kelimeler:** Kopma, asimetrik daralma, aksi-simetrik damla deformasyonu  
Stokes akışı, sınır integral denklemleri, sınır elemanı metodu

*To my beloved ones.*

# Acknowledgment

I am indebted to my advisor, Dr. Umut Ceyhan, for his selfless support in my studies, for always contributing to my development and instilling a love of learning in me. I would not have been able to accomplish this work without his excellent guidance and friendship.

I would like to thank my committee members Dr. Sercan Acarer and Dr. Mehmet Akif Ezan for their interests and valuable contributions.

I also would like to acknowledge all my friends who were always there when I need their knowledge and their support. Last but not least, I want to thank my parents, who are my greatest luck, for their unconditional support and understanding.

# Table of Contents

Declaration of Authorship .....	ii
Abstract .....	iii
Öz .....	iv
Acknowledgment .....	vi
List of Figures .....	ix
List of Tables.....	xi
List of Symbols .....	xii
<b>1 Introduction .....</b>	<b>1</b>
<b>2 Mathematical Formulation .....</b>	<b>6</b>
<b>3 Numerical Method.....</b>	<b>9</b>
3.1 Boundary Integral Equations .....	9
3.2 Axisymmetric Formulation.....	13
3.3 Boundary Element Method.....	16
3.4 Solver Validation .....	20
3.4.1 Mesh Independence .....	20
3.4.2 Time Step .....	22
3.4.3 Validation: Flow in Straight Capillaries .....	22
<b>4 Flow in tubes with asymmetric constrictions.....</b>	<b>26</b>
<b>5 Comparison the Plane Flow with Axisymmetric Deformation .....</b>	<b>32</b>
<b>6 Conclusion .....</b>	<b>35</b>
<b>References .....</b>	<b>36</b>
<b>Appendices .....</b>	<b>42</b>



Appendix A Treatment of Singular Integrals .....	43
Appendix B Two-Dimensional Boundary Integrals .....	45
<b>Curriculum Vitae .....</b>	<b>48</b>

# List of Figures

Figure 2.1	Domain of the problem .....	7
Figure 3.1	Representative cubic elements on drop boundary .....	17
Figure 3.2	Change of drop profile with $N_d$ .....	21
Figure 3.3	Evolution of a drop with time; $r_{eff} = 0.9, \lambda = 0.1, Ca = 1$ . The solid lines represent the present results, and square symbols represent the data of Tsai and Miksis [19] .....	23
Figure 3.4	Extra pressure drop as a function of drop size; —: $Ca = 0.075$ , — — — : $Ca = 0.10$ , — · — : $Ca = 0.15$ are present results; ····· : theoretical expression of Brenner [42]. The symbols represent the experimental results of Ho and Leal [14] ○: $Ca = 0.075$ ; □: $Ca = 0.10$ ; ◇: $Ca = 0.15$ .....	24
Figure 3.5	Film thickness as a function of $Ca$ ; ○: $\lambda = 1$ [16]; ◇: $\lambda = 0.1$ [19]; □: $\lambda = 0$ [2]; solid and dashed lines represent the present results for $\lambda = 1$ , and $\lambda = 0.1$ , respectively.....	25
Figure 4.1	Effect of $r_d$ and $r_u$ on drop snap-off. panel (a) is for unit $r_d$ and $r_u$ , panels (b)-(d) are for $r_u = 1, r_d = 1.5, 2$ , and $2.5$ , respectively, panels (e)-(g) are for $r_d = 1, r_u = 1.5, 2$ , and $2.5$ , respectively .....	28
Figure 4.2	Variation of volume of the generated droplet after snap-off with smoothness of upstream and downstream.....	29
Figure 4.3	Effect of asymmetry due to downstream radius of curvature: top half is for a symmetric constriction with $R_u = R_d = 1$ , drop profiles at $t = 0$ (—), 2 (— — —), 4 (— · —), 6 (—); bottom half is for an asymmetric constriction with $R_u = 1$ ; $R_d = 1.5$ , drop profiles at $t = 0$ (—), 2 (— — —), 4 (— · —), 4.164 (—); .....	30
Figure 4.4	History of pressure drop across tube and stages of drop deformation mechanism through constriction, dashed line corresponds to symmetric constriction with no snap-off while the dot-dash line corresponds to asymmetric constriction shown in Figure 4.3. ....	31

Figure 5.1	Deformation of drops for axisymmetric flow (top), and plan flow (bottom); $r_{eff} = 0.9, \lambda = 0.1, Ca = 1$ .....	33
Figure 5.2	Deformation of drop through a symmetric constriction; drop profiles at at $t = 0, 0.5, 0.913, 2.5$ for axisymmetric flow (top) and $t = 0, 0.25, 0.4565, 1.25$ for plane flow (bottom) .....	34

# List of Tables

Table 3.1	Change of the dimensionless maximum drop length in the axial direction with $N_d$ .....	21
-----------	--	----

# List of Symbols

$\alpha$	Viscosity ratio for drop or suspending fluid
$\gamma$	Interfacial tension between drop and suspending fluid [N/m]
$\Gamma$	Domain boundary
$\delta$	Kronocker delta
$\Delta$	Difference
$\varepsilon$	Coefficient of $\mathbf{c}$ for drop or suspending fluid
$\eta$	Dynamic viscosity of suspending fluid [Pa.s]
$\theta$	Response point angle
$\kappa$	Surface curvature
$\lambda$	Viscosity ratio of drop to suspending fluid
$\xi$	Arclength parameter
$\pi$	Pi number
$\boldsymbol{\sigma}$	Stress tensor
$\varphi$	Shape function
$\phi$	Source point angle
$\Omega$	Fluid domain
$a$	Elliptic integral variable ( $r^2 + R^2 + c^2$ )
$A$	Rotation matrix
$b$	Elliptic integral variable ( $2Rr$ )
$\mathbf{b}$	Constant vector defining the strength and orientation of point force
$c$	Elliptic integral variable ( $Z - z$ )

$\mathbf{C}$	Principle value tensor
$Ca$	Capillary number ( $\eta u_s/\gamma$ )
$d$	Elliptic integral variable ( $-rn_r + cn_z$ )
$e$	Elliptic integral variable ( $R^2 + r^2$ )
$\mathbf{e}$	Unit vector
$E(k)$	Elliptic integral of second kind
$\mathbf{f}$	Traction
$\mathbf{G}$	Fundamental solution for velocity
$h$	Height of the plane channel [m]
$\mathbf{I}$	Identity tensor
$J$	Jacobian
$k$	Elliptic integral variable ( $\sqrt{2b/a + b}$ )
$K(k)$	Elliptic integral of first kind
$l_s$	Length scale
$N$	Number of elements
$p$	Pressure [N/m <sup>2</sup> ]
$p_s$	Pressure scale
$p^+$	Extra pressure
$q$	Pressure (3.2) [N/m <sup>2</sup> ]
$Q$	Volumetric flow rate [m <sup>3</sup> /s]
$r$	Magnitude of the distance between source and field point
$\mathbf{r}$	Radial coordinate, field point
$\hat{\mathbf{r}}$	Distance between source and field point
$r_d$	Major axis of the downstream
$r_{eff}$	Effective drop radius
$r_u$	Major axis of the upstream
$r_t$	Throat radius

<b><math>R</math></b>	Radial coordinate, source point
$R_0$	Radius of the capillary tube [m]
$R_d$	Radius of the downstream of the tube [m]
$R_u$	Radius of the upstream of the tube [m]
$s$	Arc length along the generating curve
$t$	Time [s]
$t_s$	Time scale
<b><math>T</math></b>	Fundamental solution for stress
<b><math>u</math></b>	Velocity [m/s]
$u_s$	Velocity scale
<b><math>v</math></b>	Velocity (3.2)
$\mathcal{V}_d$	Volume of the daughter droplet generated after snap-off
$\mathcal{V}_i$	Initial volume of the drop
<b><math>x</math></b>	Source point
<b><math>X</math></b>	Interface position
<b><math>y</math></b>	Field point
<b><math>z</math></b>	Axial coordinate, field point
$z_0$	Axial location of the center of ellipses generating the asymmetric constriction
<b><math>Z</math></b>	Axial coordinate, source point

### Subscripts

$\beta$	Drop or suspending fluid
$d$	Drop
$s$	Suspending fluid
$in$	Tube inlet

<i>out</i>	Tube outlet
<i>w</i>	Capillary wall
<i>z</i>	Axial component



# Chapter 1

## Introduction

The motion of drops and bubbles through capillary tubes and microchannels is of great interest in multiphase flow in porous media, microfluidic devices, and lab-on-a-chip applications [1-8]. Due to the small length scales in the aforementioned problems, the motion is, generally, in creeping flow regime. In all these applications, it is important to define and estimate the effect of geometric and physical parameters on drop behavior for the design and control purposes. The physical parameters that determine the flow characteristics are the viscosity ratio ( $\lambda$ ) of drop and suspending fluid, the effective radius of the drop ( $r_{eff}$ ) and the capillary number ( $Ca$ ) which defines the ratio of viscous forces that tend to deform drops to interfacial forces that act to maintain the initial shape.

The investigation of the dependence of drop behavior on physical parameters is initiated by Fairbrother and Stubbs [9] who study on large inviscid drops, as known as bubbles, and find that the thickness of the thin film between the tube wall and the bubble interface scales to be  $Ca^{1/2}$  for  $Ca$  up to 0.014. Taylor [10] performs experiments as an extension of the previous study for larger capillary numbers and shows that the expression is valid for  $Ca < 0.09$ . Similarly, Bretherton [11] predicts the film profile of large bubbles by lubrication theory. He finds that the film thickness and the extra pressure drop are functions of capillary number and scales as  $Ca^{2/3}$ . He propounds that the discrepancy between the scales is due to the difference between theory and experiments. Goldsmith and Mason [12, 13] evaluate the film thickness and the velocity profiles inside and outside the drops at very low viscosity ratios. They also observe breakup of sufficiently large drops at both ends of the drop due to the nonuniform film thinning [13]. Ho and Leal [14] perform a comprehensive experimental study on the influence of physical parameters on drop deformation, drop

velocity, and the extra pressure drop. The film thickness is found to be independent of the drop volume for  $r_{eff} > 1$ , but increases with the volume for  $r_{eff}$  up to unity. It is also affected by the viscosity ratio and the capillary number, i.e. the drop elongates in the flow direction as  $\lambda$  and  $Ca$  increases. The drop velocity and the extra pressure drop are affected by the drop shape. The wall effects become significant as the film thickness decreases leading the drop velocity to decrease. The extra pressure drop depends on the drop shape but its dependence on the drop volume changes with the viscosity ratio. The replacement of the suspending fluid with a more viscous fluid causes higher pressure drop, while less viscous fluid causes lower pressure drop. Westborg and Hassager [15] examine the film thickness for the flow of bubbles and viscous drops using finite element method. Their results agree well with the expressions of Bretherton [11] and they note that the film thickness is independent from the viscosity ratio at small capillary number. Martinez and Udell [16] use boundary element method to study the effect of physical parameters on extra pressure drop and drop velocity. Their results agree well with the experimental results of Ho and Leal [14]. Olbricht and Kung [17] experimentally study the deformation and breakup mechanism of a drop in a circular tube. They report the critical capillary number depending on the viscosity ratio and drop size that leads the breakup. The shape of the drop strongly depends on the capillary number for viscous drops but becomes less sensitive for the smaller viscosity ratio. They observe that for sufficiently large capillary number, the drop does not reach the steady state shape. Lac and Sherwood [18] study the drop deformation in a wide range of capillary number using boundary element method. For all capillary numbers, the extra pressure drop becomes independent from the drop volume as the volume increases, for unit viscosity ratio. They also observe the breakup at high capillary number due to jet forming at the rear end as mentioned in the earlier studies [13, 17, 19].

The physical mechanism behind these motions is more complex in channel geometries having constrictions and/or expansions. Change in the channel radius is often used to force the drops and bubbles to breakup and/or coalesce. Understanding these mechanisms is required for the design and control of systems including such constrictions and/or expansions. Snap-off is one of the breakup mechanisms that is observed while drops and bubbles are passing through the constriction, due to the collar formation of outer wetting fluid around the drop. The pressure difference due to

the low pressure in the constricted region forces the suspending fluid to move towards the constriction. As a result, the collar that started to form in the constriction continues to grow until the drop breaks. Thus, the snap-off time is directly proportional with the rate of collar formation. Roof [20] shows that the snap-off time can be reduced by opening a groove in the capillary wall so that the wetting fluid has an additional path. Olbricht and Leal [21] carry out experiments to study the motion of drops flowing through a periodically constricted capillary. The shape and the pressure drop variations over time are reported. The drops with larger radius than the capillary promotes negative extra pressure drop while they are passing through the constrictions. They report that under the same flow conditions with straight capillary, breakup may occur in constricted capillary. Gauglitz et al. [22] study the snap-off of large bubbles in a constricted capillary and they measure the breakup time as a function of capillary number. Later, Gauglitz and Radke [23] develop a small-slope theory to study on the collar formation by a wetting liquid film. They also perform experiments, and the results show an agreement with the theory. Martinez and Udell [24] study the same problem [21] using boundary element method and observe similar results except for the breakup. The collar growth depends on the film thickness, so implicitly on the capillary number. At low capillary numbers, the coated film thickness is thin, and the drop leaves the constriction until the necessary amount of collar is formed for the snap-off to occur. As the capillary number directly affects the drop velocity, at high capillary numbers, even if the film thickness is sufficient for snap-off, snap-off cannot be observed in this case as the drop leaves the constriction fast. Tsai and Miksis [19] simulate the problem for low viscosity drops since more viscous drops are more resistant to deform, and snap-off does not occur at high viscosity ratios. In addition to their results, geometric parameters such as the depth and length of the constriction affect the snap-off. The depth of the constriction determines whether the snap-off would occur or not, but the length only affects the snap-off time and the effective radius of the daughter droplet. Snap-off of a large oil drop immersed in water flowing through a constricted capillary studied experimentally by Peña et al. [25]. They show that as viscosity ratio increases, the shear stress at the interface becomes significant and the flow rate of the continuous phase decreases. Thus, if the drop viscosity is much larger than the suspending fluid viscosity ( $\lambda \gg 1$ ), snap-off does not occur. The occurrence of snap-off and its time are found to be directly relevant with the flow rate.

Roman et al. [26] perform numerical and experimental studies to investigate the breakup of large bubbles in a constricted tube. They report the period of snap-off/coalescence events by measuring the film thickness and correlated it with the capillary number. Zhang et al. [27] study on the prediction of snap-off of a drop in a constricted channel. They present a diagram which shows the dependency of the snap-off on viscosity ratio and  $Ca$  and find a criterion for the occurrence of snap-off as a function which states at large viscosity ratio and/or large  $Ca$ , snap-off does not occur. They also investigate the viscous dissipation rate during the snap-off and observe that the snap-off is related to a sudden increase in viscous dissipation. Very low capillary numbers are considered with the smallest order of  $10^{-6}$  as in [25]. Huang et al. [28] simulate the flow of a drop due to gravity through a single circular constriction at non-zero Reynolds numbers. Unlike other studies [19, 25, 27], they observe that higher drop viscosity gives the continuous phase sufficient time to cause breakup due to its relatively lower velocity to the continuous phase. Lately, Singla and Ray [29] review the previous studies and describe and suggest the effect of physical parameters, as well as geometric parameters, in other words surface topography, on drop deformation.

In pore geometries with circular cross sections, Roof's criterion for snap-off states that the capillary pressure across the meniscus in the pore body should be less than the local pressure at the pore throat which is proportional to the throat geometry. Studies influenced by this criterion [30-34] consider symmetric constrictions, however, asymmetry, is natural in a porous medium or can be used in microfluidic channels to control the drop breakup processes. Therefore, we construct an asymmetric single constriction consisting of two ellipses with different major axes and show that the snap-off mechanism depends on the asymmetry of the constriction as much as the previously stated physical parameters. For this model problem, which requires relocating the interface at each time step, boundary element method is preferable since it provides the discretization of the boundaries only, and determination of the unknown values by using the information on the boundary nodes. Due to its advantages mentioned, boundary element method is found to be ideal for the solution of the axisymmetric problem of this thesis.

Mathematical formulation for the model problem including the governing equations and tube geometry is given in Chapter 2. Problem related axisymmetric boundary

integral equations are derived, the numerical implementation and the verification studies are presented in Chapter 3. In Chapter 4, we represent the flow of drop through asymmetric constriction and compare the axisymmetric deformation with plane flow in Chapter 5. We conclude our findings and give the contribution of thesis in Chapter 6.

# Chapter 2

## Mathematical Formulation

In this chapter, we derive a mathematical model describing the motion of a drop in a capillary tube. We consider a drop with effective radius  $r_{eff}$  and dynamic viscosity  $\lambda\eta$  in a capillary tube of radius  $R_0$ , suspended in another fluid with dynamic viscosity  $\eta$  as shown in Figure 2.1. The coordinate is fixed on the stationary tube inlet with symmetry axis  $z$ , and radial axis  $r$ . We treat the fluids to be incompressible, neutrally buoyant, and immiscible. The inlet and outlet boundaries of the domain are  $\Gamma_{in}$  and  $\Gamma_{out}$ , the capillary wall is  $\Gamma_w$  ( $\Gamma_{in} \cup \Gamma_{out} \cup \Gamma_w = \Gamma$ ), and the drop interface is  $\Gamma_d$  with  $\mathbf{n}$  being the unit normal into the suspending fluid. Non-dimensionalized with scales  $l_s = R_0$ ,  $u_s = Q/(\pi R_0^2)$ ,  $t_s = l_s/u_s$ ,  $p_s = \eta u_s/l_s$  with  $Q$  being the volume flow rate, the continuity equation requires that the divergence of the velocity vanishes:

$$\nabla \cdot \mathbf{u} = 0 \quad (2.1)$$

where  $\mathbf{u}$  is the non-dimensional velocity field. In this flow, due to the small length and velocity scales, the Reynolds number indicating the ratio between inertia and viscous forces is small ( $Re \ll 1$ ). Therefore, we assume the inertial terms can be neglected and flow is governed by the Stokes equations of motion which requires the stress field is divergenceless:

$$\nabla \cdot \boldsymbol{\sigma} = 0 \quad (2.2)$$

where the constitutive law for the Cauchy stress tensor in (2.2) is defined for incompressible Newtonian fluids as

$$\boldsymbol{\sigma} = -p\mathbf{I} + \alpha(\nabla\mathbf{u} + \nabla\mathbf{u}^T) \quad (2.3)$$

where  $p$  is the pressure. In (2.3),  $\alpha$  is  $\lambda$  which is the viscosity ratio, for the drop ( $\Omega_d$ ) and 1 for the suspending fluid ( $\Omega_s$ ). The velocity along the tube wall satisfies the no-slip and no-penetration condition.

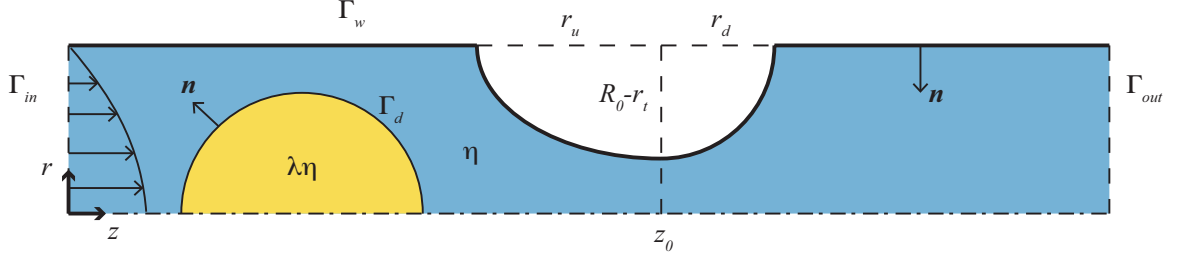


Figure 2.1: Domain of the problem

We specify a parabolic velocity profile that the suspending fluid satisfies Poiseuille flow when it is sufficiently far ahead and behind the drop as

$$\mathbf{u} = 2(1 - r^2)\mathbf{e}_z \quad \text{on } \Gamma_{in} \cup \Gamma_{out}. \quad (2.4)$$

The normal stress balance, in its dimensionless form, at the drop interface requires

$$(\boldsymbol{\sigma}_s - \boldsymbol{\sigma}_d) \cdot \mathbf{n} = \Delta \mathbf{f} = \frac{1}{Ca} (\nabla \cdot \mathbf{n}) \mathbf{n} \quad (2.5)$$

where  $\Delta \mathbf{f}$  denotes the traction jump across the interface;  $Ca (= \eta u_s / \gamma)$  is based on the suspending fluid dynamic viscosity  $\eta$  and its average velocity scale  $u_s$  and the surface tension denoted by  $\gamma$  is assumed to be uniform and the velocity is continuous ( $\mathbf{u}_s = \mathbf{u}_d$ ) at the interface. The interface moves normal to itself, and we define the kinematic condition with  $\mathbf{X}$  denoting the interface position by

$$\mathbf{u} \cdot \mathbf{n} = \frac{\partial \mathbf{X}}{\partial t} \cdot \mathbf{n} \quad \text{on } \Gamma_d. \quad (2.6)$$

As shown in Figure 2.1, the generating curve of the constriction is obtained by combining two ellipses with the same minor axes at  $z_0$ , but different major axes; this provides us with the asymmetric constriction with respect to  $z_0$ . The minor axis,  $r_c$ , is along  $r$  direction and it determines the throat radius  $r_t$ , while the major axes,  $r_u$  and  $r_d$  are along  $z$ .

In this problem, we are mainly interested in the evolution of the fluid interface. In parallel with this purpose, we solve the continuity (2.1) and the Stokes equations (2.2) with the boundary conditions (2.4) - (2.6) to find the drop velocity for the determination of the drop shape through the kinematic condition (2.6) and the traction on the capillary.



# Chapter 3

## Numerical Method

This chapter presents the boundary element method for the solution of the model problem. The theory and the reformulation of the governing equations into boundary integral equations are given in §3.1. The transformation of the surface integrals into line integrals for axisymmetric formulation is explained, and the components of the fundamental solutions are given in §3.2. The tube and the drop boundaries are discretized and approximated in §3.3. The independence study from number of boundary elements and the time step, and the validation of the numerical solver is presented in §3.4.

### 3.1 Boundary Integral Equations

The motion and the deformation of drops through tubes are governed by the continuity equation (2.1) and the Stokes equations (2.2). Boundary integral formulation of Stokes flow is developed by using Lorentz reciprocal relation that considers two unrelated Newtonian flows with velocity fields  $u_j$  and  $u_j'$  and associated stress fields  $\sigma_{ij}$  and  $\sigma_{ij}'$

$$u_j' \frac{\partial \sigma_{ij}}{\partial x_i} - u_j \frac{\partial \sigma_{ij}'}{\partial x_i} = \frac{\partial}{\partial x_i} (u_j' \sigma_{ij} - u_j \sigma_{ij}'). \quad (3.1)$$

The Green's functions of Stokes flow provide us with velocity and stress fields that satisfy the continuity equation, and the singularly forced Stokes equation

$$\nabla \cdot \boldsymbol{\sigma} = -\nabla p + \nabla^2 \mathbf{u} + \delta(\mathbf{x} - \mathbf{y}) \mathbf{b} \quad (3.2)$$

where  $\delta$  is Kronocker delta. Green's functions physically specify the velocity field at point  $\mathbf{y}$  due to a point force of magnitude and orientation  $\mathbf{b}$ , applied at the source point  $\mathbf{x}$ . The solutions of (3.2) are

$$\mathbf{u}(\mathbf{y}) = \frac{1}{8\pi} \mathbf{G}(\mathbf{x}, \mathbf{y}) \mathbf{b}, \quad (3.3a)$$

$$\boldsymbol{\sigma}(\mathbf{y}) = \frac{1}{8\pi} \mathbf{T}(\mathbf{x}, \mathbf{y}) \mathbf{b}. \quad (3.3b)$$

$\mathbf{G}$  and  $\mathbf{T}$  are free space Green's functions for velocity and stress, respectively, and given by

$$G_{ij}(\mathbf{x}, \mathbf{y}) = \frac{\delta_{ij}}{r} + \frac{\hat{r}_i \hat{r}_j}{r^3} \quad (3.4a)$$

$$T_{ij}(\mathbf{x}, \mathbf{y}) = -6 \frac{\hat{r}_i \hat{r}_j \hat{r}_k}{r^5} \quad (3.4b)$$

where  $\hat{\mathbf{r}} = \mathbf{x} - \mathbf{y}$  and  $r = |\hat{\mathbf{r}}|$ .

To derive the boundary integral equation of three-dimensional Stokes flow, we apply the relation (3.1) for a Stokes flow with velocity  $u_j$  and stress  $\sigma_{ij}$  and use fundamental solutions similar to those given in (3.3) for  $u'_j$  and  $\sigma'_{ij}$ , and we obtain

$$\delta(\mathbf{x}, \mathbf{y}) b_j u_j(\mathbf{y}) = \frac{\partial}{\partial x_i} \left( \frac{1}{8\pi} G_{ij}(\mathbf{x}, \mathbf{y}) b_j \sigma_{ij}(\mathbf{y}) - u_j(\mathbf{y}) \frac{1}{8\pi} T_{ijk}(\mathbf{x}, \mathbf{y}) b_j \right). \quad (3.5)$$

Simplifying for an arbitrary vector  $\mathbf{b}$ , the equation becomes

$$\delta(\mathbf{x}, \mathbf{y}) u_j(\mathbf{y}) = \frac{1}{8\pi} \frac{\partial}{\partial x_i} \left( G_{ij}(\mathbf{x}, \mathbf{y}) \sigma_{ij}(\mathbf{y}) - u_j(\mathbf{y}) T_{ijk}(\mathbf{x}, \mathbf{y}) \right). \quad (3.6)$$

We integrate this equation over the control domain  $\Omega$  bounded by  $\Gamma$  and using the divergence theorem to convert the volume integrals into surface integrals we obtain

$$\mathbf{C}(\mathbf{x})\mathbf{u}(\mathbf{x}) = \frac{1}{8\pi} \int_{\Gamma} \mathbf{G}(\mathbf{x}, \mathbf{y}) \mathbf{f}(\mathbf{y}) dS(\mathbf{y}) - \frac{1}{8\pi} \int_{\Gamma} \mathbf{u}(\mathbf{y}) \mathbf{T}(\mathbf{x}, \mathbf{y}) \mathbf{n}(\mathbf{y}) dS(\mathbf{y}). \quad (3.7)$$

The first integral in (3.7) is called single layer potential and the second is called double layer potential. The density of the single layer potential,  $\mathbf{u}$ , is continuous everywhere in the domain while the density of the double layer potential,  $\mathbf{f}$ , is discontinuous.  $\mathbf{C}$  on the left-hand side of (3.7) is the principal value tensor, obtained by using the property of delta function, expressing the discontinuity of the potential of double layer. The left hand-side of (3.7) is  $\mathbf{u}(\mathbf{x})$  when the point  $\mathbf{x}$  lies inside the domain  $\Omega$  and zero when the point  $\mathbf{x}$  lies outside the boundary  $\Gamma$ .

Since we deal with multiphase flow, the general boundary integral equation (3.7) is rearranged for our problem which contains two fluid domains and an interface. To derive the boundary integrals, we first consider the suspending fluid bounded by  $\Gamma$  and contains  $\Gamma_d$  (see Figure 2.1). The integral equation is written as

$$\begin{aligned} & -\frac{1}{8\pi} \int_{\Gamma \cup \Gamma_d} \mathbf{G}(\mathbf{x}, \mathbf{y}) \mathbf{f}_s(\mathbf{y}) dS(\mathbf{y}) + \frac{1}{8\pi} \int_{\Gamma \cup \Gamma_d} \mathbf{u}_s(\mathbf{y}) \mathbf{T}(\mathbf{x}, \mathbf{y}) \mathbf{n}(\mathbf{y}) dS(\mathbf{y}) \\ & = \begin{cases} \mathbf{C}(\mathbf{x})\mathbf{u}_s(\mathbf{x}), & \mathbf{x} \in \Gamma \cup \Gamma_d \\ \mathbf{u}_s(\mathbf{x}), & \mathbf{x} \in \Omega_s \\ 0, & \mathbf{x} \in \Omega_d \end{cases}. \end{aligned} \quad (3.8)$$

We decide the right hand-side of the equation with respect to the location of the source point. It equals to  $\mathbf{C}(\mathbf{x})\mathbf{u}_s(\mathbf{x})$  when the source point lies on the boundary and  $\mathbf{C}(\mathbf{x})$  equals to  $\frac{1}{2}\mathbf{I}$  for a smooth boundary.

To obtain the boundary integral equation for drop bounded by  $\Gamma_d$ , we follow similar analysis, and the resulting equation is

$$\begin{aligned}
& -\frac{1}{8\pi\lambda} \int_{\Gamma_d} \mathbf{G}(\mathbf{x}, \mathbf{y}) \mathbf{f}_d(\mathbf{y}) dS(\mathbf{y}) + \frac{1}{8\pi} \int_{\Gamma_d} \mathbf{u}_d(\mathbf{y}) \mathbf{T}(\mathbf{x}, \mathbf{y}) \mathbf{n}(\mathbf{y}) dS(\mathbf{y}). \\
& = \begin{cases} \mathbf{C}(\mathbf{x}) \mathbf{u}_d(\mathbf{x}), & \mathbf{x} \in \Gamma_d \\ 0, & \mathbf{x} \in \Gamma \cup \Omega_s \\ \mathbf{u}_d(\mathbf{x}), & \mathbf{x} \in \Omega_d \end{cases} \quad (3.9)
\end{aligned}$$

The coupled integral equation related to the velocity at each point on the tube and drop boundaries is derived by taking the corresponding values of the right hand-side for each fluid domain. To simplify the equations, we first multiply (3.9) with  $\lambda$ . When the source point,  $\mathbf{x}$ , is on  $\Gamma$ , we take the summation of the first equation of (3.8) and the second equation of (3.9). Since the integrals of (3.8) are on  $\Gamma \cup \Gamma_d$ , while summation, we utilize the condition that the velocity is continuous on the interface, ( $\mathbf{u}_s = \mathbf{u}_d$  on  $\Gamma_d$ ), but the traction difference leads a stress jump across the interface as given in (2.5), since  $\mathbf{f}_s$  does not equal to  $\mathbf{f}_d$  on the drop interface. Following the same analysis, when the source point is on  $\Gamma_d$ , we sum the first equations of (3.8) and (3.9). After the rearrangements, we obtain the boundary integral equation for two-phase flow

$$\begin{aligned}
\varepsilon \mathbf{C}(\mathbf{x}) \mathbf{u}_\beta(\mathbf{x}) &= -\frac{1}{8\pi} \int_{\Gamma} \mathbf{G}(\mathbf{x}, \mathbf{y}) \mathbf{f}_s(\mathbf{y}) dS(\mathbf{y}) \\
&+ \frac{1}{8\pi} \int_{\Gamma} \mathbf{u}_s(\mathbf{y}) \mathbf{T}(\mathbf{x}, \mathbf{y}) \mathbf{n}(\mathbf{y}) dS(\mathbf{y}) \\
&- \frac{1}{8\pi} \frac{1}{Ca} \int_{\Gamma_d} \mathbf{G}(\mathbf{x}, \mathbf{y}) (\nabla \cdot \mathbf{n}(\mathbf{y})) \mathbf{n}(\mathbf{y}) dS(\mathbf{y}) \\
&+ \frac{(1-\lambda)}{8\pi} \int_{\Gamma_d} \mathbf{u}_d(\mathbf{y}) \mathbf{T}(\mathbf{x}, \mathbf{y}) \mathbf{n}(\mathbf{y}) dS(\mathbf{y}). \quad (3.10)
\end{aligned}$$

In (3.10),  $\varepsilon$  is  $(1 + \lambda)$  when  $\beta$  is  $d$ , and 1 when  $\beta$  is  $s$ .

### 3.2 Axisymmetric Formulation

The boundary integral formulation for three-dimensional flow is given in §3.1. For the axisymmetric case, the point force in three-dimensions expresses a unit force equally distributed around a ring. To determine the response at point  $\mathbf{y}$ , the axisymmetric fundamental solutions are derived by integrating the three-dimensional solution (3.4) about a ring at point  $\mathbf{x}$ . Therefore, for the axisymmetric problem, the surface integrals reduce to line integrals by computing the azimuthal integrals analytically. For the treatment of the axisymmetric problem, we consider the cylindrical coordinates in which the points are  $\mathbf{x} = (R, \theta, Z)$  and  $\mathbf{y} = (r, \phi, z)$ . The solutions in cylindrical coordinates are determined by tensor transformation

$$\mathbf{u}(\mathbf{x}) = \mathbf{A}^T(\mathbf{x})\mathbf{u}(\mathbf{x}, \mathbf{y})\mathbf{A}(\mathbf{y}) \quad (3.11)$$

where  $\mathbf{A}$  is the rotation matrix for field point and  $\mathbf{A}^T$  is transpose of  $\mathbf{A}$  corresponding to source point:

$$\mathbf{A}(\mathbf{y}) = \begin{bmatrix} \cos\phi & -\sin\phi & 0 \\ \sin\phi & \cos\phi & 0 \\ 0 & 0 & 1 \end{bmatrix}, \quad (3.12a)$$

$$\mathbf{A}^T(\mathbf{x}) = \begin{bmatrix} \cos\theta & \sin\theta & 0 \\ -\sin\theta & \cos\theta & 0 \\ 0 & 0 & 1 \end{bmatrix}. \quad (3.12b)$$

For an arbitrary plane we choose  $\phi$  to be zero, and the mapping from cartesian coordinates  $\mathbf{x} = (x, y, z)$  to cylindrical coordinates is  $\mathbf{x} = (x_r \cos\theta, x_r \sin\theta, x_z)$ .

We integrate the transformed solutions about the ring

$$u_{rr} = \int_0^{2\pi} [(u_{11}\cos\theta + u_{21}\sin\theta)\cos\phi + (u_{12}\cos\theta + u_{22}\sin\theta)\sin\phi] d\phi \quad (3.13a)$$

$$u_{rz} = \int_0^{2\pi} (u_{31}\cos\phi + u_{32}\sin\phi)d\phi \quad (3.13b)$$

$$u_{zr} = \int_0^{2\pi} (u_{13}\cos\theta + u_{32}\sin\theta)d\phi \quad (3.13c)$$

$$u_{zz} = \int_0^{2\pi} u_{33}d\phi \quad (3.13d)$$

and after we compute the integrals, we obtain the axisymmetric fundamental solutions for velocity [47] as follows:

$$u_{rr} = \frac{1}{2\pi\sqrt{\bar{a} + \bar{b}}} \left[ -\left(\frac{\bar{a} + \bar{c}^2}{\bar{b}}\right) K(k) + \left(\frac{\bar{b}^2 - \bar{a}^2 - \bar{a}\bar{c}^2}{\bar{b}}\right) \frac{E(k)}{\bar{a} - \bar{b}} \right], \quad (3.14a)$$

$$u_{rz} = \frac{1}{2\pi\sqrt{a + b}} \left[ \left(\frac{cr}{b}\right) K(k) + \left(\frac{cR - acr}{b}\right) \frac{E(k)}{a - b} \right], \quad (3.14b)$$

$$u_{zr} = \frac{1}{2\pi\sqrt{a + b}} \left[ -\left(\frac{cR}{b}\right) K(k) + \left(\frac{-cr + acR}{b}\right) \frac{E(k)}{a - b} \right], \quad (3.14c)$$

$$u_{zz} = \frac{1}{2\pi\sqrt{a + b}} \left[ K(k) + (c^2) \frac{E(k)}{a - b} \right]. \quad (3.14d)$$

where  $a = R^2 + r^2 + c^2$ ,  $b = 2Rr$ ,  $c = Z - z$ , and  $k = [2b/(a + b)]^{1/2}$ .  $K(k)$  and  $E(k)$  are the elliptic integrals of the first and second kind, respectively [48]. Applying the same procedure gives us the fundamental solutions for tractions in cylindrical coordinate system.

$$\begin{aligned}
t_{rr} = & \frac{1}{\pi(a^2 - b^2)\sqrt{a+b}} \left[ \frac{K(k)}{b^2} [db^3 + ab^2 Rn_r - 2abde \right. \\
& + (4a^2 - 6b^2)(eRn_r - dRr) - (8a^3b - 9ab^3)Rn_r] \\
& + \frac{E(k)}{(a-b)2b^2} [-4ab^3d + (a^2b + 3b^3)(2de - bRn_r) \\
& \left. + 4a(3b^2 - a^2)(eRn_r - dRr) + (8a^4 - 15a^2b^2 + 3b^4)Rn_r] \right], \tag{3.15a}
\end{aligned}$$

$$\begin{aligned}
t_{rz} = & \frac{1}{\pi(a^2 - b^2)\sqrt{a+b}} \left[ \frac{K(k)}{2b} [-2Rbdc - 2ac(R^2n_r - rd)] \right. \\
& - (2a^2 - 3b^2)cn_r] + \frac{cE(k)}{b(a-b)} [-4Rabd \\
& \left. + (a^2 + 3b^3)(R^2n_r - rd) + 2a(3b^2 - a^2)n_r] \right], \tag{3.15b}
\end{aligned}$$

$$\begin{aligned}
t_{zr} = & \frac{1}{\pi(a^2 - b^2)\sqrt{a+b}} \left[ \frac{cK(k)}{b^2} [rb^2d - abR(d - rn_r) \right. \\
& + (2a^2 - 3b^2)R^2n_r] + \frac{cE(k)}{b^2(a-b)} [-4rab^2d \\
& \left. + (a^2 + 3b^3)(Rd - Rrn_r) + 2a(3b^2 - a^2)R^2n_r] \right], \tag{3.15c}
\end{aligned}$$

$$\begin{aligned}
t_{zz} = & \frac{1}{\pi(a^2 - b^2)\sqrt{a+b}} \left[ \frac{K(k)}{b} [-bc^2d - aRc^2n_r] \right. \\
& \left. + \frac{E(k)}{b(a-b)} [4abdc^2 + (a^2 + 3b^3)Rc^2n_r] \right] \tag{3.15d}
\end{aligned}$$

where  $d = -rn_r + cn_z$ , and  $e = R^2 + r^2$ . The above equations (3.14) and (3.15) are the fundamental solutions to be used in the boundary integral equation (3.10).

### 3.3 Boundary Element Method

As a discretization method based on the advantages mentioned, we choose boundary element method for the solution of the boundary integral equations. Boundary element method is first used for Stokes flow by Youngren and Acrivos [35] for flow past an arbitrary particle and then introduced for the interface problems [36, 37] in unbounded domains. The method is then applied to the motion of drops and bubbles in confinements [16, 18, 19, 24, 38-46].

Boundary element method requires reformulation of the boundary integral equations into a set of linear equations by discretizing the boundary into small segments called boundary elements. The choice of the elements is problem specific. The elements may be treated as constant, linear, quadratic, or higher order. Constant elements contain one boundary node located at the midpoint of the element, linear elements contain two nodes at the extreme points of the elements, quadratic and higher order elements contains three and more boundary nodes, respectively. The known and unknown variables on the boundaries are approximated by interpolation functions between the boundary nodes. In the case of constant interpolation, a variable defined at the node is assumed to be constant along the element. Higher order interpolations provide higher accuracy, as sharing nodes will have an impact on more neighboring nodes. We choose constant elements for the fixed capillary walls regarding to computational cost, since we are mainly concerned with the evolution of the interface deformation. Another reason for choosing constant elements for the capillary wall is to avoid corner nodes where the unit normal vector is not unique. On the tube wall, we define the velocity components, and the traction components are calculated. Since traction is a function of the normal vector, the normal vector at the corner node causes confusion. Though it can be treated for higher order elements, the use of constant elements prevents this confusion. If sufficient number of constant elements are used, we do not need to consider corner nodes, which degrade the smoothness of the boundary without affecting the accuracy of the solution. For the fluid interface, we use cubic elements which involves four boundary nodes within each element as schematically shown in Figure 3.1.



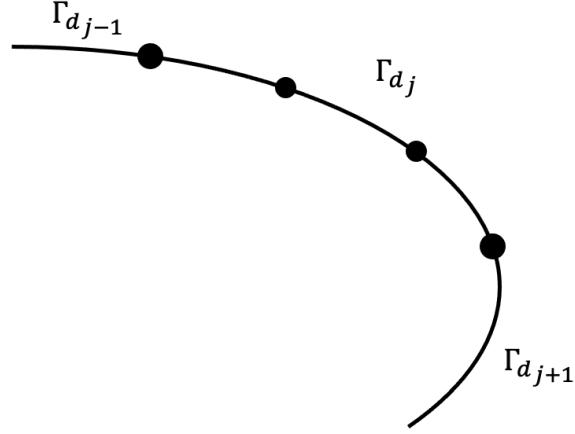


Figure 3.1: Representative cubic elements on drop boundary

We approximate the coordinates of the interface with cubic shape functions and perform the calculations on the mapped domain. The coordinates on the mapped domain are

$$\mathbf{r}(\xi) = \sum_{j=1}^4 \varphi_j^c r_j \quad (3.16a)$$

$$\mathbf{z}(\xi) = \sum_{j=1}^4 \varphi_j^c z_j \quad (3.16b)$$

where  $r_j$  and  $z_j$  are the coordinates of the node point with respect to the arclength  $\xi$  in  $[-1,1]$ , and  $\varphi_j^c$  are the cubic shape functions defined by

$$\varphi_1^c(\xi) = -(9/16)(\xi + 1/3)(\xi - 1/3)(\xi - 1) \quad (3.17a)$$

$$\varphi_2^c(\xi) = (27/16)(\xi + 1)(\xi - 1/3)(\xi - 1) \quad (3.17b)$$

$$\varphi_3^c(\xi) = -(27/16)(\xi + 1)(\xi + 1/3)(\xi - 1) \quad (3.17c)$$

$$\varphi_4^c(\xi) = (9/16)(\xi - 1/3)(\xi + 1/3)(\xi + 1) \quad (3.17d)$$

The velocity and traction components are also approximated by the cubic shape functions as

$$\mathbf{u}(\xi) = \sum_{j=1}^4 \varphi_j^c u_j, \quad (3.18a)$$

$$\mathbf{t}(\xi) = \sum_{j=1}^4 \varphi_j^c t_j. \quad (3.18b)$$

Beside the interface, since we use constant elements for the capillary walls, each element has one node and the shape function  $\varphi$  is unity. Therefore, we divide the tube boundary into  $N$  elements and the drop boundary into  $N_d$  elements which have  $N$  and  $3N_d + 1$  boundary nodes, respectively. The resulting linear system is obtained by summing the integrals for each element as below

$$\begin{aligned} \begin{bmatrix} C_{rr} & C_{rz} \\ C_{zr} & C_{zz} \end{bmatrix}_{ii} \begin{bmatrix} u_r \\ u_z \end{bmatrix}_i &= (1 - \lambda) \sum_{j=1}^{N_d} \int_{\Gamma_{d_j}} \begin{bmatrix} T_{rr} & T_{rz} \\ T_{zr} & T_{zz} \end{bmatrix}_{ij} \begin{bmatrix} u_r \\ u_z \end{bmatrix}_j d\Gamma \\ &+ \sum_{j=1}^N \int_{\Gamma_j} \begin{bmatrix} T_{rr} & T_{rz} \\ T_{zr} & T_{zz} \end{bmatrix}_{ij} \begin{bmatrix} u_r \\ u_z \end{bmatrix}_j d\Gamma \\ &- \sum_{j=1}^N \int_{\Gamma_j} \begin{bmatrix} G_{rr} & G_{rz} \\ G_{zr} & G_{zz} \end{bmatrix}_{ij} \begin{bmatrix} f_r \\ f_z \end{bmatrix}_j d\Gamma \\ &- \frac{\nabla \cdot \mathbf{n}}{Ca} \sum_{j=1}^{N_d} \int_{\Gamma_{d_j}} \begin{bmatrix} G_{rr} & G_{rz} \\ G_{zr} & G_{zz} \end{bmatrix}_{ij} \begin{bmatrix} n_r \\ n_z \end{bmatrix}_j d\Gamma \end{aligned} \quad (3.19)$$

where  $d\Gamma$  is the differential line element given by

$$d\Gamma = r(s) \left[ \left( \frac{dr}{ds} \right)^2 + \left( \frac{dz}{ds} \right)^2 \right]^{1/2}, \quad (3.20)$$

and  $s$  is the arclength along the generating curve.

The components of the unit normal vectors are

$$n_z = \frac{\frac{dr}{ds}}{\left[ \left( \frac{dr}{ds} \right)^2 + \left( \frac{dz}{ds} \right)^2 \right]^{1/2}}, \quad (3.21a)$$

$$n_r = \frac{\frac{dz}{ds}}{\left[ \left( \frac{dr}{ds} \right)^2 + \left( \frac{dz}{ds} \right)^2 \right]^{1/2}}. \quad (3.21b)$$

The surface curvature along the drop boundary has two contributions: one plane curvature and one azimuthal curvature:

$$\nabla \cdot \mathbf{n} = \kappa_z + \kappa_r = \frac{\frac{dr}{ds} \frac{d^2z}{ds^2} - \frac{dz}{ds} \frac{d^2r}{ds^2}}{\left[ \left( \frac{dr}{ds} \right)^2 + \left( \frac{dz}{ds} \right)^2 \right]^{3/2}} + \frac{\frac{dz}{ds}}{r \left[ \left( \frac{dr}{ds} \right)^2 + \left( \frac{dz}{ds} \right)^2 \right]^{1/2}}. \quad (3.22)$$

Because the evaluation of the surface curvature requires the second order derivatives of the axial and radial coordinates, to ensure the continuity of the curvature, we use cubic-spline interpolation. We start with  $N/2$  elements and mirror the coordinates with respect to the symmetry axis which ends up with closed curve with  $N$  elements (as periodic treatment). In the cubic spline notation, the  $j$ th boundary element ( $j = 1, 2, \dots, N$ ) between the nodes of  $j$  and  $j + 1$  is parametrically defined with cubic polynomials

$$x_j(s) = a_{x_j}s^3 + b_{x_j}s^2 + c_{x_j}s + d_{x_j} \quad (3.23a)$$

$$y_j(s) = a_{y_j}s^3 + b_{y_j}s^2 + c_{y_j}s + d_{y_j} \quad (3.23b)$$

The coefficients are computed by implementing the interpolation and smoothness conditions. For each element, we have 8 unknowns ( $a, b, c, d$  for  $x$  and  $y$  coordinates) with a total of  $8N$  unknowns. We, first, enforce the first and last coordinates for  $j$ th

element which gives us  $4N$  equations. Next, we ensure the continuity of first and second derivatives at the first and last nodes of  $jth$  element which gives us  $2N$  equations for slope and  $2N$  equations for curvature.  $8N$  equations close the problem.

## 3.4 Solver Validation

### 3.4.1 Mesh Independence

Before verifying the numerical solver, independence from number of boundary elements must be ensured. To do so, we solve two problems. For the first comparison, we solve the motion of a drop of effective radius 1.1 in a straight capillary at  $Ca = 0.1$ , and  $\lambda = 0.19$  and compare the dimensionless length of the steady state profile of a drop with varying  $N_d$  in Table 3.1. The length of the drop is calculated as 1.54 from the result of Martinez and Udell [16]. We also make sure the volume of the drop is conserved; in all of the numerical experiments, the relative error in the drop volume is kept less than 0.1%. The relative error between the solutions used  $N_d = 120$  and  $N_d = 180$  is 0.0015%, and the error between  $N_d = 360$  and  $N_d = 420$  is 0.0091%.

For the second comparison, we solve the deformation of a drop at  $Ca = 1$  by varying  $N_d$  from 15 to 360 as shown in Figure 3.2.

Therefore, we use 120 cubic elements when the drop deformation is relatively small (e.g. deformation of drops in straight tubes for  $Ca < 1$ ), and 360 elements when the deformation is relatively large (e.g. snap-off problem).

Table 3.1: Change of the dimensionless maximum drop length in the axial direction with  $N_d$

$N_d$	$L_d/2r_{eff}$
15	1.5545
30	1.5512
45	1.5502
60	1.5497
90	1.5494
120	1.5490
180	1.5490
240	1.5489
300	1.5489
360	1.5488
420	1.5488

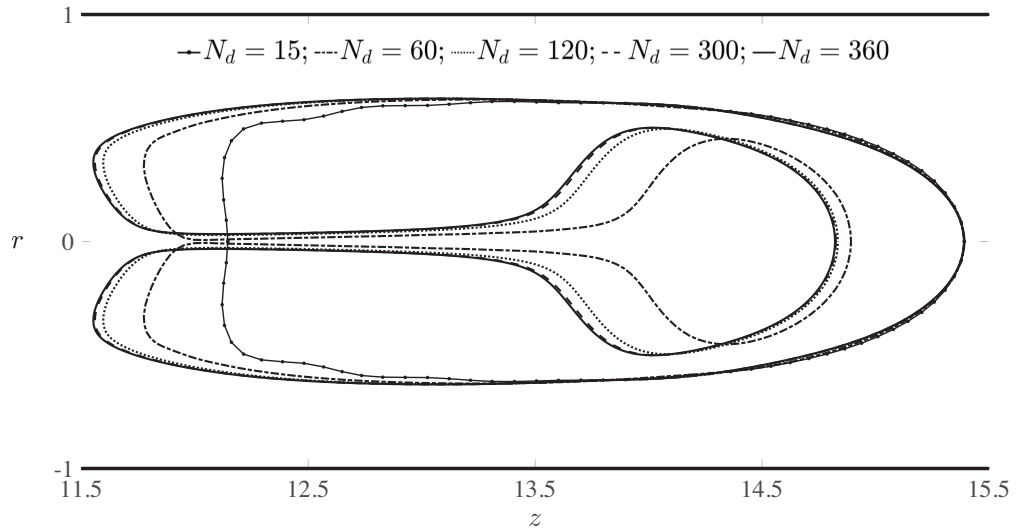


Figure 3.2: Change of drop profile with  $N_d$

### 3.4.2 Time Step

Although the Stokes equations of motion are linear and not time dependent, the unsteadiness is due to the non-linear evolution of the interface with time. The time integration was performed using first order Euler formula (2.6) by dynamically determining the time step not to allow a boundary node moves more than a tolerance. We define the initial time step as  $5 \times 10^{-4}$  and if maximum displacement of a node is larger than the tolerance, we do not accept the solution and decrease the time step.

### 3.4.3 Validation: Flow in Straight Capillaries

One of the fundamental problems of drop motion in confined geometries is the deformation of drops in straight tubes. Though this problem is studied widely, we separate this section to such problems to validate our solver. For the first problem, we analyze the deformation of a drop in a straight tube with jet formation behind if a critical  $Ca$  is reached. This phenomenon is observed experimentally by Olbricht and Kung [17] and later simulated by Tsai and Miksis [19]. This unsteady problem provides a check for the abrupt interface variation to capture if the curvature and integral computations are implemented correctly, any blemish in either of the computations cannot capture such deformations. To this end, we set the initial drop effective radius to 0.9 and  $Ca$  to unity and let the drop evolve from its spherical shape centered at  $z = 2$  in time until the leading edge reaches the tube outlet. We plot our observation of jet formation at  $Ca = 1$  in which the drop does not reach steady-state and compare with Tsai and Miksis [19] at different times as shown in Figure 3.1 at  $t = 0, 2, 4, 6$ . At this  $Ca$ , the surface tension forces at the trailing edge of the drop cannot overcome the viscous forces, the curvature there changes sign, and a reentrant cavity grows as jet towards the leading edge of the drop. At around  $t = 6$ , the jet gets so thin that its interface nearly touches the symmetry axis around which we stop the simulations. Further integration in time for the physics of such coalescences needs the addition of other effective forces, such as van-der-Waals, into (3.11) at this length scale.

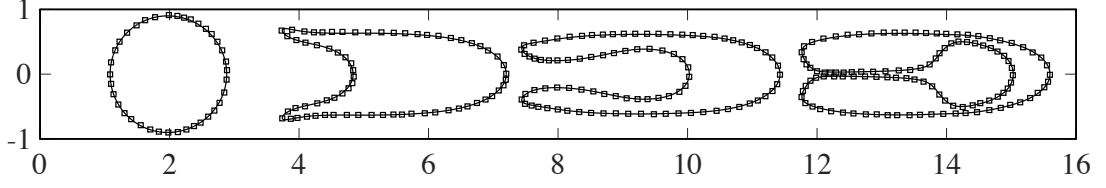


Figure 3.3: Evolution of a drop with time;  $a = 0.9$ ,  $\lambda = 0.1$ ,  $Ca = 1$ . The solid lines represent the present results, and square symbols represent the data of Tsai and Miksis [19]

As a second problem, we consider the motion of drops reaching steady-state profiles to be able to compare our results with other flow parameters such as extra pressure drop due to the existence of drop inside tubes and thickness of suspending liquid coated on the tube walls other than drop profiles. To reach their steady-state profiles and not to be affected by the tube ends, the drops are held at the middle of a tube of length  $L = 20R$  by shifting their center of mass to the mid of the tube at each time step. The extra pressure drop due to the existence of a drop in the tube is the pressure drop difference of the case with the drop moving in the tube and the one with no drop for fixed volume flow rate. It is experimentally and computationally observed that the less viscous drop than its surrounding causes a negative extra pressure drop while more viscous drop causes a positive extra pressure drop [14, 17, 18]. In Figure 3.4, we compare extra pressure drop due to the existence of drops with experiments of Ho and Leal [14], and the limiting case given by Brenner [49] for small drops for different  $Ca$ ,  $\lambda$ , and  $r_{eff}$ . We vary the effective drop radius from 0.7 to 1.1 and measure the extra pressure drops for  $Ca = 0.075, 0.1, 0.15$  and  $\lambda = 0.19, 2.04$ . We observe similar trends for  $\lambda < 1$  and  $\lambda > 1$  with experiments. The deviation between the present and experimental results is also observed by Martinez and Udell [16] with which our computations match. This discrepancy is also mentioned by the experimental study of Olbricht and Kung [17] in which they compare the steady-state non-dimensional drop length (scaled with the twice of the effective drop radius) with the numerical computation of Martinez and Udell [16] for  $\lambda = 0.19, Ca = 0.1, r_{eff} = 1.1$ . While the experimentally measured length is 1.5, the computed value is 1.55 which is also consistent with our results.

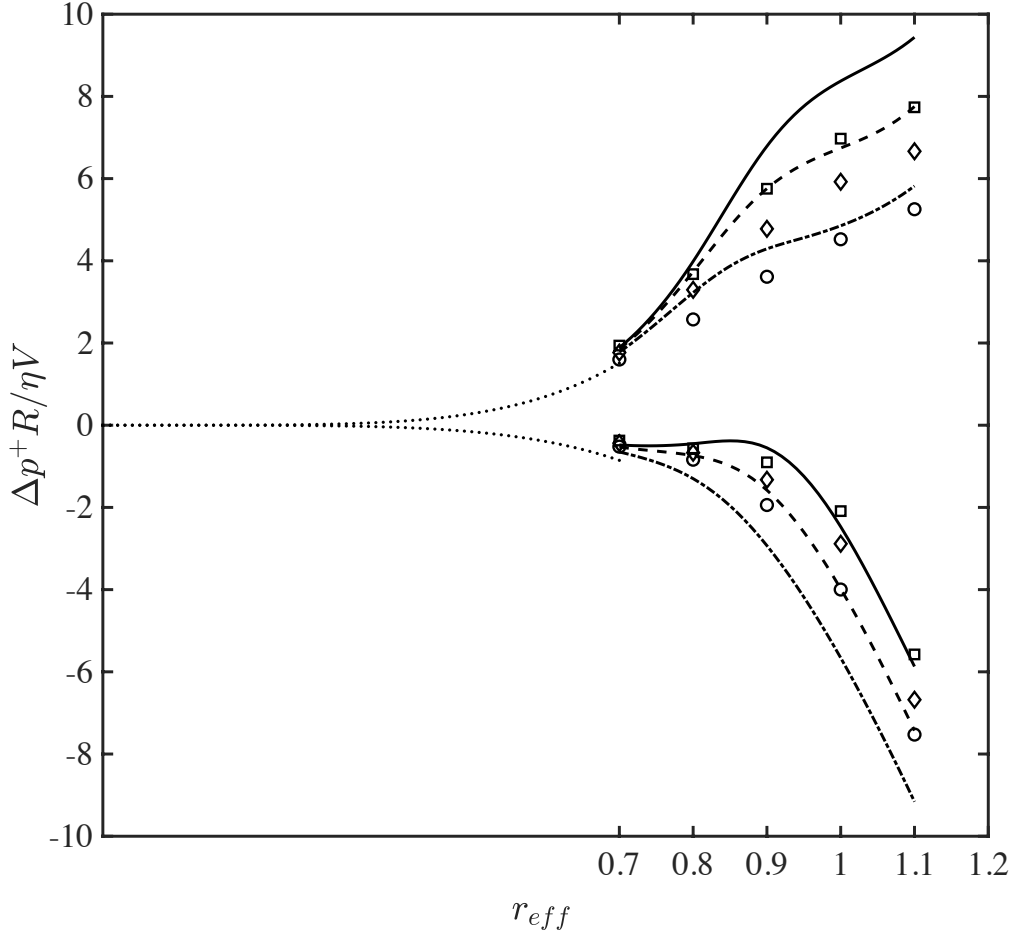


Figure 3.4: Extra pressure drop as a function of drop size: —:  $Ca = 0.075$ , ---:  $Ca = 0.10$ , - · - · -:  $Ca = 0.15$  are present results; ..... : theoretical expression of Brenner [49]. The symbols represent the experimental results of Ho and Leal [14] ○:  $Ca = 0.075$ ; □:  $Ca = 0.10$ , ◇:  $Ca = 0.15$

As a final comparison, we measure the coated film thickness on tube walls as a function of  $Ca$  and compare with Martinez and Udell [16] ( $\lambda = 0.19$ , and  $\lambda = 1$ ), Tsai and Miksis [19], ( $\lambda = 0.1$ ), and Taylor [2] in Figure 3.5. The comparison for  $\lambda = 0.19$  is not included in the figure for simplicity which is also studied in §3.4.1. Taylor [2] defined the  $Ca$  as a function of drop velocity, so for the comparison, the given data have been taken according to the suspending fluid velocity. As the viscosity ratio approaches zero, the film thickness decreases, and results approximate the film thickness measurements for bubbles. We should also note that, for the unit viscosity ratio, when  $Ca$  is higher than 0.15, we do not observe film formation.



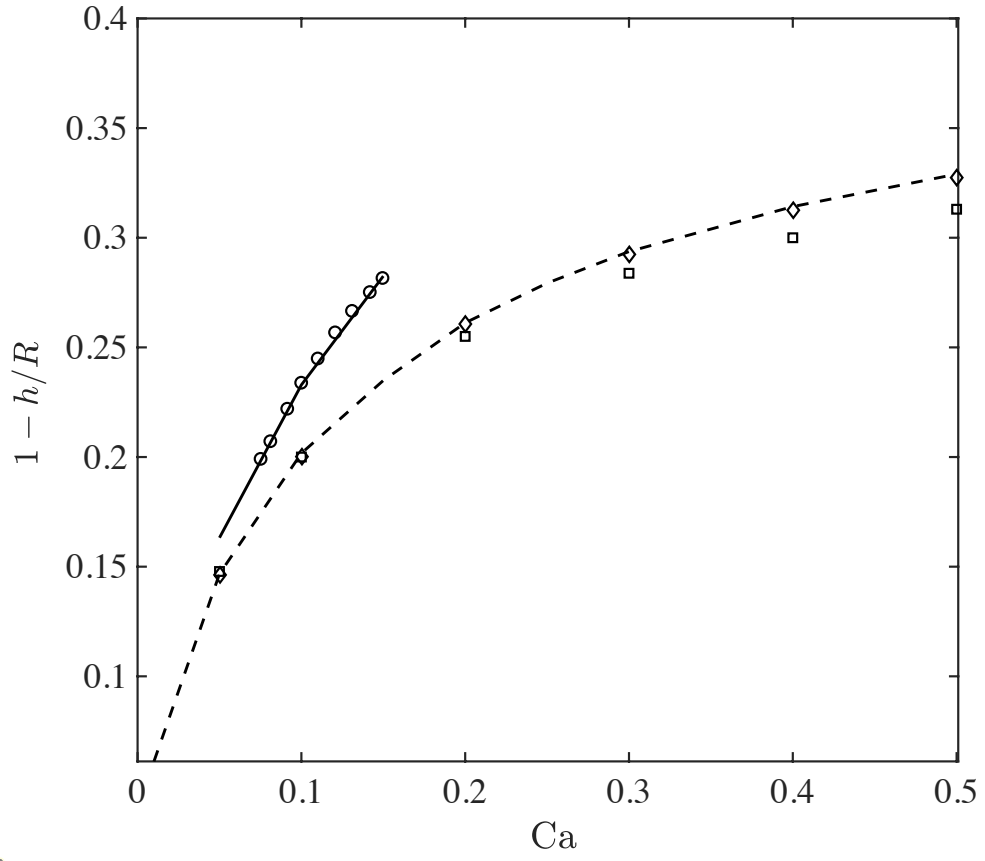


Figure 3.5: Film thickness as a function of  $Ca$ ;  $\circ$ :  $\lambda = 1$  [16];  $\diamond$ :  $\lambda = 0.1$  [19];  $\square$ :  $\lambda = 0$  [10]; solid and dashed lines represent the present results for  $\lambda = 1$ , and  $\lambda = 0.1$ , respectively

## Chapter 4

# Flow in tubes with asymmetric constrictions

The drop deformation mechanism is greatly influenced by the existence of constrictions in confined geometries. As the drop passes through the constriction, breakup may occur as a result of the growth of the suspending fluid collar. The breakup that occurs in this way is called snap-off. This mechanism is affected by  $Ca$ ,  $\lambda$ ,  $r_{eff}$  and the geometry of constriction. The studies either in small slope regime or Stokes regime [19, 20 - 27] consider periodic or single but symmetric constriction effects on the drop deformation. Asymmetry, however, is natural in a porous medium or can be used in microfluidic channels to control the drop breakup processes. To observe the effect of asymmetry, we construct an isolated asymmetric constriction. As shown in Figure 2.1, the generating curve of the constriction is obtained by combining two ellipses with the same minor axes at  $z_0$ , but different major axes; this provides us with an asymmetric constriction with respect to  $z_0$ . The minor axis,  $r_c$  is along  $r$  direction and it determines the throat radius,  $r_t$ , while the major axes,  $r_u$  and  $r_d$ , are along  $z$ . We initiate the motion of drops upstream of the constriction with an initial drop profile corresponding to the steady-state profiles in a straight tube of length 12 and place their leading-edge at  $z = z_0 - r_u - 0.25$ .

Our starting point is a case in which we observe snap-off and then we vary the geometry. We, first, fix the viscosity ratio to  $\lambda = 0.005$ ,  $Ca = 0.05$ , and effective drop radius to  $r_{eff} = 1.1$ . The drop snaps-off when the upstream and downstream radii of the constriction are  $r_u = r_d = 1.0$  and  $r_c = 0.6$ . We, systematically, vary the major axis ( $r_d$ ) of the downstream of the constriction from  $r_d = 1$  to  $r_d = 2.5$  while keeping

all other parameters fixed and plot the drop profiles at the time of snap-off for different  $r_d$  in Figure 4.1.

For cases (a)-(d), drop fronts start at the same axial locations from, and snap-off time is a measure of the effect of asymmetry. As  $r_d$  increases, the downstream of the constriction diverges smoothly and this extends the time for the drop front to have a maximum radius of curvature. For small  $\lambda$ , the drop can be thought of as a bubble and the pressure jump across the drop interface increases faster at the leading edge while the shape of the trailing edge remains almost the same. The interface curvature at the throat is also determined by the fixed  $r_t$  and the principal radii of curvature of the interface. Locally, at the throat, the capillary pressure has a lower bound in the limit as film thickness goes to zero: the dimensionless pressure is  $1/r_t - 1/(1 - r_t)$  which is 0.833 for  $r_t = 0.4$ . As the film thickens within this region, the corresponding pressure may exceed the leading edge which is also bounded by confinement of the tube wall ( $\sim 2$ ), of course, in the small  $Ca$  limit. In this situation, the collar grows, and the process is slower for smoother downstream, and this mechanism leads to faster snap-off: volume of the drop generated increases with smoother diverging constriction. The location of the snap-off position, on the other hand, moves downstream. The experiments of Roof [20] show that an irregularity in the pore is necessary for the snap-off to happen in a reasonable amount of time. Our results are consistent with this observation.

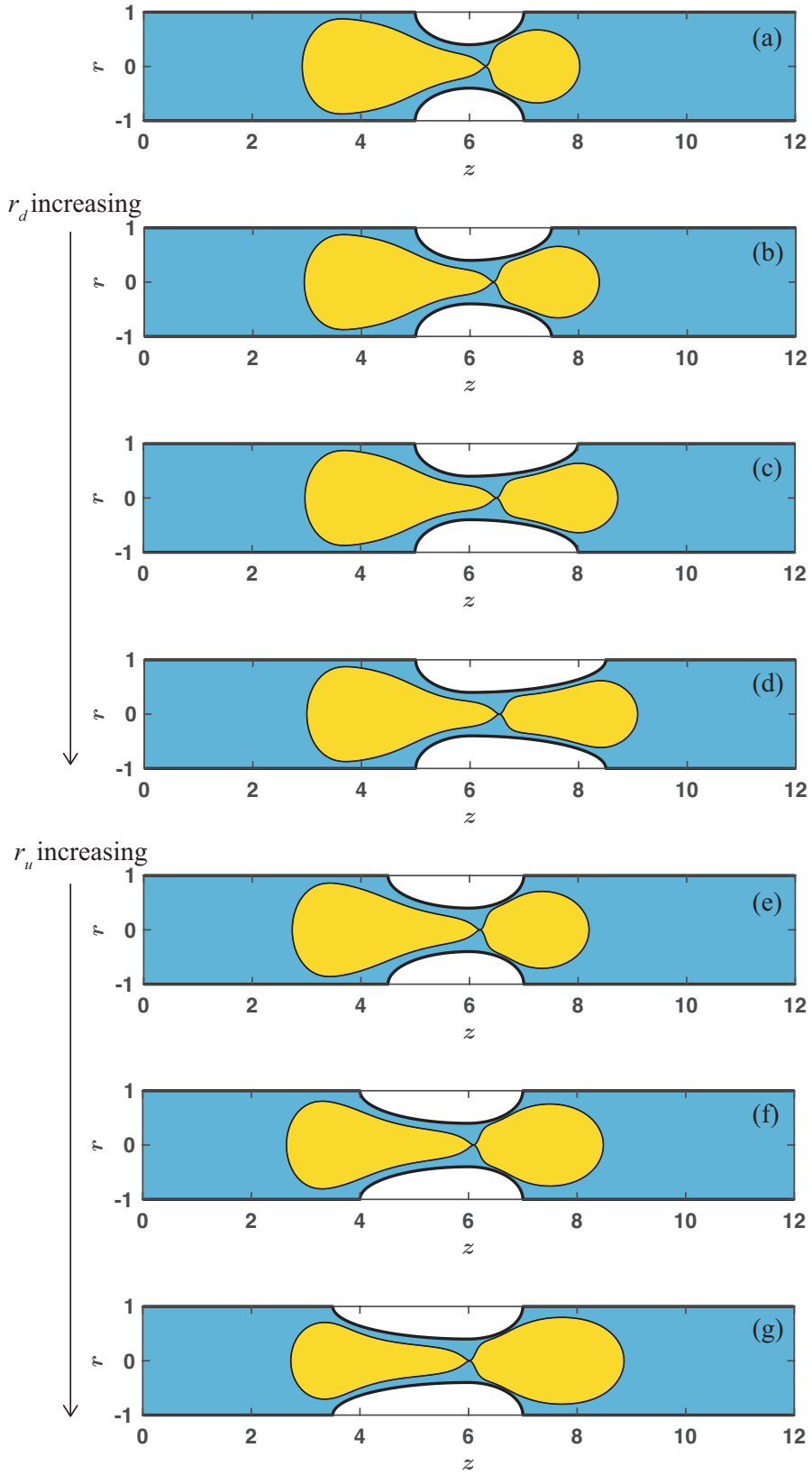


Figure 4.1: Effect of  $r_d$  and  $r_u$  on drop snap-off. Panel (a) is for unit  $r_d$  and  $r_u$ , panels (b)-(d) are for  $r_u = 1$ ,  $r_d = 1.5, 2$ , and  $2.5$ , respectively, panels (e)-(g) are for  $r_d = 1$ ,  $r_u = 1.5, 2$ , and  $2.5$ , respectively

The smoothness of the upstream of the constriction, however, is dominant for the control of the volume of the generated droplet,  $\mathcal{V}_d$ , after snap-off. We show this variation in Figure 4.1 ((e)-(g)) and plot the variation of this volume relative to initial drop volume,  $\mathcal{V}_i$ , with  $r_u$ , for fixed  $r_d = 1$  and  $r_t = 0.4$  in Figure 4.2. The smooth entrance to the constriction provides more volume to move downstream before the leading edge of the drop starts expanding and this mechanism generates more volume after snap-off.

For comparison, we also show on the same graph, the volume variation with  $r_d$ ; it is evident that volume is affected more by the smoothness of the upstream. To see the effect of upstream geometry, we replace the upstream half of the constriction with a linearly varying profile instead of an ellipse and observe similar trends. Our argument on asymmetric constriction could be used to control drop generation.

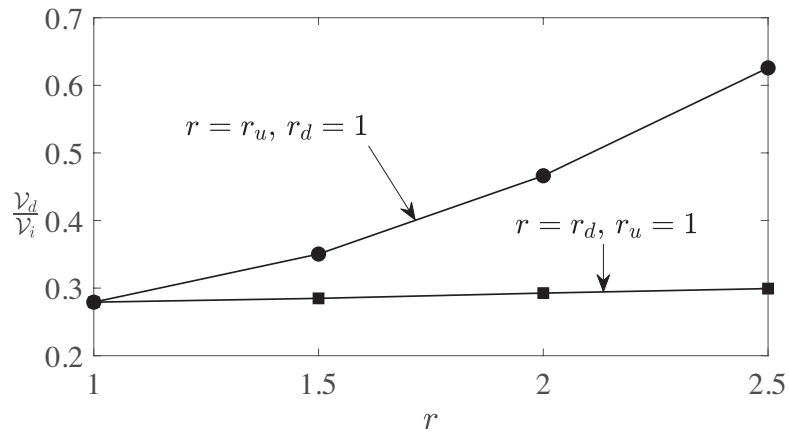


Figure 4.2: Variation of volume of the generated droplet related to after snap-off with smoothness of upstream and downstream

We should also note that the above argument holds as long as the variation in the upstream radius of curvature of the drop is small compared to the one at the throat and downstream. This condition can easily be satisfied by increasing the volume of the initial drop. The time scale for the collar growth needs to be smaller from both time scales of the variation in the leading and trailing edges.

We further consider various cases in which drops do not snap off and show that increasing downstream of the tube leads drops to snap off as the leading edge of the drop grows beyond the limits of the upstream radius of curvature of the tube. When the leading edge of the drop is allowed to expand beyond the limits of the upstream

radius of curvature, a drop, which is able to escape from the constriction with  $r_u = r_d = 1.0$ , can snap-off. We show this by increasing the radius of the tube downstream to  $R_d = 1.5$  and compare it with the symmetric case in Figure 4.3. Here, the viscosity ratio is  $\lambda = 0.0075$ ,  $Ca = 0.025$  and  $r_c = r_t = 0.5$ .

We start both cases with a drop of effective radius  $r_{eff} = 1.5$  and plot the time series of the drop profiles. The profiles at times  $t = 2$  are alike, after this time the asymmetry allows expansion. The increase of the upstream radius of curvature increases the radius of curvature of the leading edge of the drop which results with snap-off, albeit larger  $\lambda$  and throat radius, smaller  $Ca$ ; all of which tends to prevent snap-off.

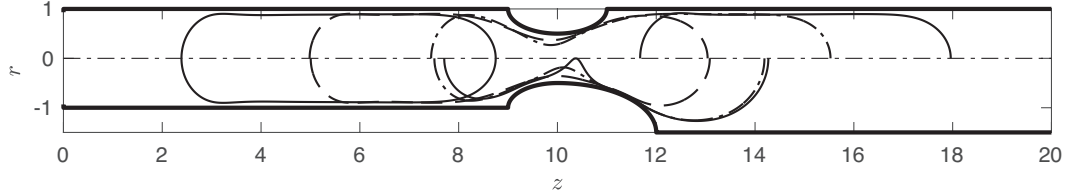


Figure 4.3: Effect of asymmetry due to downstream radius of curvature: top half is for a symmetric constriction with  $R_u = R_d = 1$ , drop profiles at  $t = 0$  (—), 2 (---), 4 (- · -), 6 (—); bottom half is for an asymmetric constriction with  $R_u = 1$ ;  $R_d = 1.5$ , drop profiles at  $t = 0$  (—), 2 (---), 4(- · -), 4.164 (—)

The history of pressure drop across the tube unveils the deformation mechanism. As shown in Figure 4.4, starting from  $t = 0$ , the pressure drop increases while the leading edge enters into the constriction. It reaches to a peak value at which the leading edge is at the narrowest section of the constriction. Here, the radius of curvature of the leading edge is at its minimum value. After this point, the leading edge starts expanding while leaving the constriction. For sufficiently large drops, we observe almost constant pressure drop ( $1.5 < t < 4$ , quasi-steady translation) as the drop retains its profile as is. In the next stage, if there is no snap-off (dashed line in Figure 4.4), the trailing edge leaves the constriction while the pressure drop decreases to a minimum which corresponds to the time at which the trailing edge is at the narrowest section, the radius of curvature of the trailing edge, this time, attains its minimum value. After this point the trailing edge expands which increases the pressure drop and reaches to quasi-steady translation. If there is snap-off (dot-dash line in Figure 4.4), the pressure drop jumps just after the plateau region (quasi-steady translation); this is

provided by the increase of the radius of the curvature at the leading edge due to asymmetry.

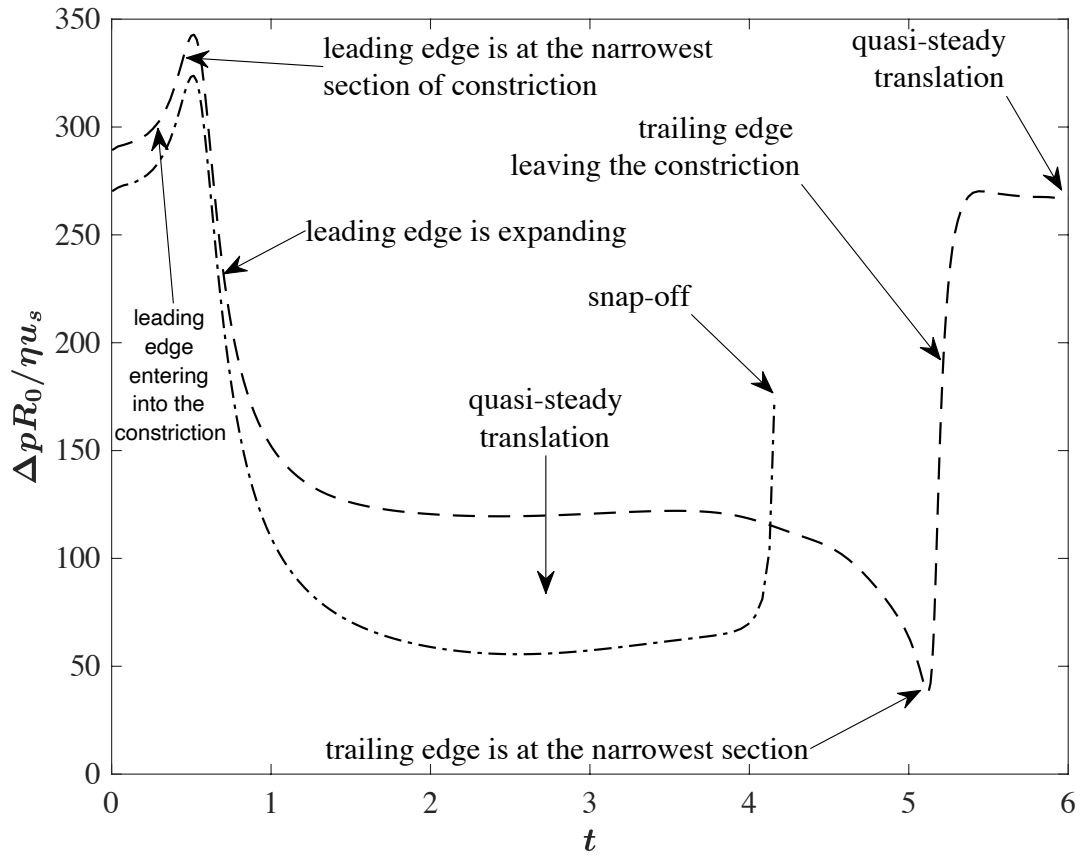


Figure 4.4: History of pressure drop across tube and stages of drop deformation mechanism through constriction, dashed line corresponds to symmetric constriction with no snap-off while the dot-dash line corresponds to asymmetric constriction shown in Figure 4.3.

# Chapter 5

## Comparison with Plane Flow

Our purpose in this section is to show the importance of azimuthal curvature on the deformation of drops; two-dimensional models may not be sufficient for models of jet formation and snap-off. For this purpose, we develop a planar version of our solver. The fundamental solutions in the two-dimensional case with corresponding boundary integral formulation are given in Appendix B. We set both cases to be dynamically and geometrically similar: setting the velocity scale  $u_s$  equal provides us with the same  $Ca$  for fixed surface tension and dynamic viscosity of the suspending fluid; namely, the volume flow rate per unit depth of the planar case averaged with channel height,  $h$ , is same as the volume flow rate of the axisymmetric one averaged with cross-sectional area. However, the time scale  $t_s = l_s/u_s$ , differs for plane and axisymmetric flows due to the different length scale. The velocity profile we set at the inlet and outlet of the channel is

$$\mathbf{u} = 6(y - y^2)\mathbf{e}_x \quad \text{on } \Gamma_{in} \cup \Gamma_{out} \quad (5.1)$$

In axisymmetric boundary element analyses, the surface curvature (3.22) has plane and azimuthal components which allow us to catch the real-like shape. In two dimensions, the curvature has only the plane component and is given as

$$\kappa = \frac{\frac{dx}{ds} \frac{d^2y}{ds^2} - \frac{dy}{ds} \frac{d^2x}{ds^2}}{\left[ \left( \frac{dx}{ds} \right)^2 + \left( \frac{dy}{ds} \right)^2 \right]^{3/2}}. \quad (5.2)$$



We first compare jet formation problem at  $Ca = 1$  given in §3.4.3. Here, the viscous forces are as much important as the surface tension forces. While a jet develops from the trailing edge of the drop in the axisymmetric case, the interface recoils in time with no jet formation in planar case. The drop speeds differ considerably. Considering the time scale  $t_s$ , the length scale is  $l_s = R_0$  for axisymmetric flow and  $l_s = 2R_0$  for plane flow. Therefore, we plot our results at  $t = 0, 1, 2$ , and 3 for plane flow and at  $t = 0, 2, 4$ , and 6 for axisymmetric flow Figure 5.1.

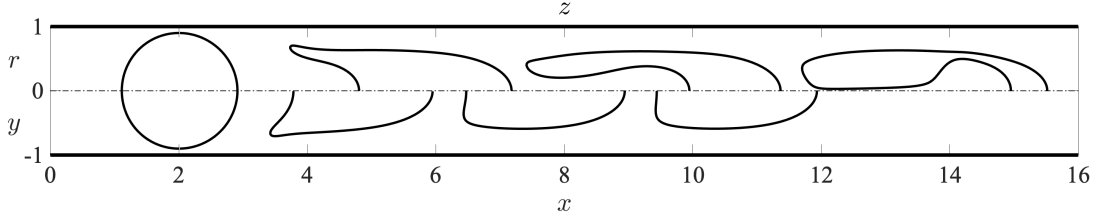


Figure 5.1: Deformation of drops for axisymmetric flow (top), and plane flow (bottom);  $r_{eff} = 0.9, \lambda = 0.1, Ca = 1$

For the snap-off problem, we compare an axisymmetric case in which we observe snap-off. The physical and geometric parameters are same as axisymmetric problem shown in panel (a) of Figure 4.1. We compare the history of axisymmetric and planar cases at times  $t = 0, 0.5, 0.913$  in Figure 5.2. We also show in this panel, planar drop profile at  $t = 2.5$  with no snap-off. In the planar case, the surface tension forces lack the out-of plane curvature, namely the azimuthal curvature contribution does not exist comparing with the axisymmetric problem and this prevents jet formation or snap-off. These two comparisons show that plane models of drop deformation in channels should be addressed with caution.

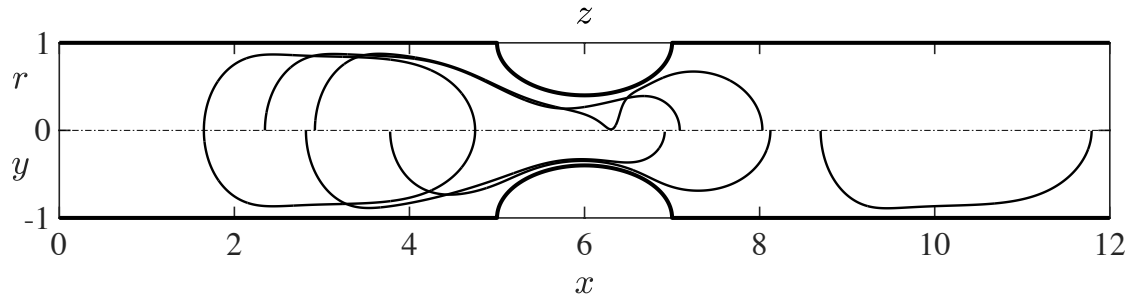


Figure 5.2: Deformation of drop through a symmetric constriction; drop profiles at  $t = 0, 0.5, 0.913, 2.5$  for axisymmetric flow (top) and  $t = 0, 0.25, 0.4565, 1.25$  for plane flow (bottom)

# Chapter 6

## Conclusion

Motivated by the lack of asymmetry effects on the drop deformation through constrictions, we develop an axisymmetric model of such deformations in creeping flow regime. In this study, rather than the role of physical parameters, our sole purpose is to show the effects of asymmetry on the snap-off mechanism. As the flow in this regime is governed by the Stokes equations of motion, we integrate the motion of drops using axisymmetric boundary integral equations. The three main conclusions of this study are as follows: (i) When we observe a snap-off in a single symmetric constriction, the asymmetry of the constriction affects the snap-off time scale. We show that the volume of the daughter droplet is mainly affected by the smoothness of the upstream of the constriction as it provides more room for the drop to fit inside the constriction before the snap-off. (ii) When we do not observe snap-off, we show that a drop may undergo break-up if the radius of the downstream of the tube is made sufficiently large to decrease the capillary pressure at the leading edge of the drop beyond the pressure at the throat. The difference between escape and snap-off of a drop can be observed from the history of pressure drop across the tube. (iii) The out-of-plane curvature contribution to the surface tension forces is crucial in the mechanism of large deformations such as jet formation and breakup. Our results contribute to the understanding of drop deformation in tubes with asymmetric constrictions and would motivate further numerical and experimental studies to control the drop deformation.

# References

- [1] Olbricht WD. Pore-scale prototypes of multiphase flow in porous media. *Annual Review of Fluid Mechanics* 1996; 28: 187-213. doi.org:10.1146/annurev.fl.28.010196.001155
- [2] Stone HA, Stroock AD, Ajdari A. Engineering flow in small devices: Microfluidics toward a lab-on-a-chip. *Annual Review of Fluid Mechanics* 2004; 36: 381-411. doi.org:10.1146/annurev.fluid.36.050802.122124
- [3] Jensen MJ, Stone HA, Bruus H. A numerical study of two-phase Stokes flow in an axisymmetric flow-focusing device. *Physics of Fluids* 2006; 18(7): 77-103. doi.org:10.1063/1.2214461
- [4] Bremond N, Thiam AR, Bibette J. Decompressing emulsion droplets favors coalescence. *Physical Review Letters* 2008; 100(2): 024501 1-4. doi.org:10.1103/PhysRevLett.100.024501
- [5] Cubaud T. Deformation and breakup of high-viscosity droplets with symmetric microfluidic cross flows. *Physical Review E* 2009; 80(2): 026307 1-4. doi.org:10.1103/PhysRevE.80.026307
- [6] Mandal A, Bera A. Modeling of flow of oil-in-water emulsions through porous media. *Petroleum Science* 2015; 12(2): 273-281. doi.org:10.1007/s12182-015-0025-x
- [7] Anna SL. Droplets and bubbles in microfluidic Devices. *Annual Review of Fluid Mechanics* 2016; 48(1): 285-309 doi.org:10.1146/annurev-fluid-122414-034425
- [8] Perazzo A, Tomaiuolo G, Preziosi V, Guido S. Emulsions in porous media: From single droplet behavior to applications for oil recovery. *Advances in Colloid and Interface Science* 2018; 256: 305-325. doi.org:10.1016/j.cis.2018.03.002

- [9] Fairbrother F, Stubbs AE. Studies in electro-endosmosis. Part VI. The “bubble-tube” method of measurement. *Journal of Chemical Sciences (Bangalore)* 1935; 119: 527-529. doi.org:10.1039/JR9350000527
- [10] Taylor GI. Deposition of a viscous fluid on the wall of a tube. *Journal of Fluid Mechanics* 1961; 10(2): 161-165. doi.org:10.1017/s0022112061000159
- [11] Bretherton FP. The motion of long bubbles in tubes. *Journal of Fluid Mechanics* 1961; 10(2): 166-188. doi.org:10.1017/S0022112061000160
- [12] Goldsmith HL, Mason SG. The movement of single large bubbles in closed vertical tubes. *Journal of Fluid Mechanics* 1962; 14(1): 42-58. doi.org:10.1017/S0022112062001068
- [13] Goldsmith HL, Mason SG. The flow of suspensions through tubes. II. Single large bubbles. *Journal of Colloid Science* 1963; 18(3): 237-261. doi.org:10.1016/0095-8522%2863%2990015-1
- [14] Ho BP, Leal LG. The creeping motion of liquid drops through a circular tube of comparable diameter. *Journal of Fluid Mechanics* 1975; 71(2): 361-383. doi.org:10.1017/S0022112075002625
- [15] Westborg H, Hassager O. Creeping motion of long bubbles and drops in capillary tubes. *Journal of Colloid and Interface Science* 1989; 133(1): 135-147. doi.org:10.1016/0021-9797%2889%2990287-7
- [16] Martinez MJ, Udell KS. Axisymmetric creeping motion of drops through circular tubes. *Journal of Fluid Mechanics* 1990; 210: 565-591. doi.org:10.1017/S0022112090001409
- [17] Olbricht WL, Kung DM. The deformation and breakup of liquid drops in low Reynolds number flow through a capillary. *Physics of Fluids A: Fluid Dynamics* 1992; 4(7): 1347-1354. doi.org:10.1063/1.858412
- [18] Lac E, Sherwood JD. Motion of a drop along the centerline of a capillary in a pressure-driven flow. *Journal of Fluid Mechanics* 2009; 640: 27-54. doi.org:10.1017/s0022112009991212

- [19] Tsai TM, Miksis MJ. Dynamics of a drop in a constricted capillary tube. *Journal of Fluid Mechanics* 1994; 274: 197-217. doi.org:10.1017/S0022112094002090
- [20] Roof JG. Snap-off of oil droplets in water-wet pores. *Society of Petroleum Engineers Journal* 1970; 10(1): 85-90. doi.org:10.2118/2504-pa
- [21] Olbricht WL, Leal LG. The creeping motion of immiscible drops through a converging/diverging tube. *Journal of Fluid Mechanics* 1983; 134: 329-355. doi.org:10.1017/S0022112083003390
- [22] Gauglitz PA, St. Laurent CM, Radke CJ. Experimental determination of gas-bubble breakup in a constricted cylindrical capillary. *Industrial & Engineering Chemistry Research* 1988; 27(7): 1282-1291. doi.org:10.1021/ie00079a032
- [23] Gauglitz PA, Radke CJ. The dynamics of liquid film breakup in constricted cylindrical capillaries. *Journal of Colloid and Interface Science* 1990; 134(1): 14-40. doi.org:10.1016/0021-9797(90)90248-M
- [24] Martinez MJ, Udell KS. Axisymmetric creeping motion of drops through a periodically constricted tube. *American Institute of Physics Conference Series* 1990; 197: 222-234. doi.org:10.1063/1.38959
- [25] Peña TJ, Carvalho MS, Alvarado M. Snap-off of a liquid drop immersed in another liquid flowing through a constricted capillary. *AIChE Journal* 2009; 55(8): 1993-1999.
- [26] Roman S, Abu-Al-Saud MO, Tokunaga T, Wan J, Kovscek AR, Tchelepi HA. Measurements and simulation of liquid films during drainage displacements and snap-off in constricted capillary tubes. *Journal of Colloid and Interface Science* 2017; 507: 279-289. doi.org:10.1016/j.jcis.2017.07.092
- [27] Zhang C, Yuan Z, Matsushita S, Xiao F, Suekane T. Interpreting dynamics of snap-off in a constricted capillary from the energy dissipation principle. *Physics of Fluids* 2021; 33(3): 032112 1-17. doi.org:10.1063/5.0044756

- [28] Huang F, Chen Z, Li Z, Gao Z, Derksen JJ, Komrakova A. Numerical study of drop behavior in a pore space. *Chemical Engineering Science* 2020; 233. doi.org:10.1016/j.ces.2020.116351
- [29] Singla A, Ray B. Effects of surface topography on low Reynolds number droplet/bubble flow through a constricted passage. *Physics of Fluids* 2021; 33(1): 011301 1-17. doi.org:10.1063/5.0031255
- [30] Ransohoff T, Gauglitz P, Radke C. Snap-off of gas bubbles in smoothly constricted noncircular capillaries. *AIChE Journal* 1987; 33: 753-765. doi.org:10.1002/AIC.690330508
- [31] Kavscek AR, Radke CJ. Gas bubble snap-off under pressure driven flow in constricted noncircular capillaries. *Colloids and Surfaces A: Physicochemical and Engineering Aspects* 1996; 117: 55-76. doi.org: 10.1016/0927-7757(96)03637-0
- [32] Kavscek AR, Radke CJ. Pressure-driven capillary snap-off of gas bubbles at low wetting-liquid content. *Colloids and Surfaces A: Physicochemical and Engineering Aspects* 2003; 212: 99-108. doi.org:10.1016/s0927-7757-2802-2900302-3
- [33] Kavscek AR, Tang GQ, Radke CJ. Verification of Roof snap off as a foam-generation mechanism in porous media at steady state. *Colloids and Surfaces A: Physicochemical and Engineering Aspects* 2007; 302(1-3): 261-260. doi.org/10.1016/j.colsurfa.2007.02.035
- [34] Deng W, Cardenas MB, Bennett PC. Extended Roof snap-off for a continuous nonwetting fluid and an example case for supercritical CO<sub>2</sub>. *Advances in Water Resources* 2014; 64: 34-46. doi.org:10.1016/j.advwatres.2013.10.001
- [35] Youngren GK, Acrivos A. Stokes flow past a particle of arbitrary shape: a numerical method of solution. *Journal of Fluid Mechanics* 1975; 69(2): 377-403. doi.org:10.1017/S0022112075001486

- [36] Youngren GK, Acrivos A. On the shape of a gas bubble in a viscous extensional flow. *Journal of Fluid Mechanics* 1976; 76(3): 433-442. doi.org:10.1017/S0022112076000724
- [37] Rallison JM, Acrivos A. A numerical study of the deformation and burst of a viscous drop in an extensional flow. *Journal of Fluid Mechanics* 1978; 89(1): 191-200. doi.org:10.1017/S0022112078002530
- [38] Khayat RE, Luciani A, Utracki LA. Boundary-element analysis of planar drop deformation in confined flow. Part 1. Newtonian fluids. *Engineering Analysis with Boundary Elements* 1997; 19(4): 279-289. doi.org:10.1016/S0955-7997-2897-2900040-4
- [39] Janssen PJA, Anderson PD. Boundary-integral method for drop deformation between parallel plates. *Physics of Fluids* 2007; 19(4): doi.org:10.1063/1.2715621
- [40] Janssen PJA, Anderson PD. A boundary-integral model for drop deformation between two parallel plates with non-unit viscosity ratio drops. *Journal of Computational Physics* 2008; 227(20): 8807-8819. doi.org:10.1016/j.jcp.2008.06.027
- [41] Wrobel LC, Soares Jr. D, Das Bhaumik CL. Drop deformation in Stokes flow through converging channels. *Engineering Analysis with Boundary Elements* 2009; 33(7): 993-1000. doi.org:10.1016/j.enganabound.2009.01.009
- [42] Pozrikidis C. Passage of a liquid drop through a bifurcation. *Engineering Analysis with Boundary Elements* 2012; 36(2): 93-103. doi.org:10.1016/j.enganabound.2011.06.009
- [43] Wang Y, Dimitrakopoulos P. Low-Reynolds-number droplet motion in a square microfluidic channel. *Theory of Computational Fluid Dynamics* 2012; 26: 361-379. doi.org:10.1007/s00162-011-0238-6
- [44] Tao J, Song X, Liu J, Wang J. Microfluidic rheology of the multiple-emulsion globule transiting in a contraction tube through a boundary element method.



Chemical Engineering Science 2013; 97: 328-336.  
doi.org:10.1016/j.ces.2013.04.043

- [45] Cunha LHP, Siqueira IR, Albuquerque EL, Oliveir TF. Flow of emulsion drops through a constricted microcapillary channel. *International Journal of Multiphase Flow* 2018; 103: 141-150.  
doi.org:10.1016/j.ijmultiphaseflow.2018.02.015
- [46] Kadivar E. Modeling droplet deformation through converging–diverging microchannels at low Reynolds number. *Acta Mechanica* 2018.
- [47] Wang K. BEM simulation for glass parisons (doctoral thesis). Eindhoven: Technische Universiteit Eindhoven; 2002.
- [48] Abramowitz M, Stegun IA. *Handbook of Mathematical Functions: with Formulas, Graphs, and Mathematical Tables*. National Bureau of Standards; 1970.
- [49] Brenner H. Pressure drop due to the motion of neutrally buoyant particles in duct flows. II. Spherical droplets and bubbles *Industrial and Engineering Chemistry Fundamentals* 1971; 10(4): 537-543. doi.org:10.1021/i160040a001
- [50] Telles JCF. A self-adaptive co-ordinate transformation for efficient numerical evaluation of general boundary element integrals. *International Journal of Numerical Methods in Engineering* 1987; 24(5): 959-973.  
doi.org:10.1002/nme.1620240509
- [51] Telles JCF, Oliviera RF. Third degree polynomial transformation for boundary element integrals: Further improvements. *Engineering Analysis with Boundary Elements* 1994; 13(2): 135-141. doi.org:10.1016/0955-7997-2894-2990016-7
- [52] Johnston PR, Elliott D. A generalization of Telles’ method for evaluating weakly singular boundary element integrals. *Journal of Computational and Applied Mathematics* 2001; 131(1-2): 223-241. doi.org:10.1016/S0377-0427(00)00273-9

# Appendices

# Appendix A

## Treatment of Singular Integrals

The kernels of the boundary integral equations contain singularity because they are function of  $r$ , the distance between source and field points. when the source point is on the same boundary element with the field point,  $r$  approaches zero and solving the singular integrals becomes a challenge. To deal with the singularity, we implement third degree polynomial transformation for the integrals, which is introduced by Telles [50], and improved by Telles and Oliveira [51].

If an integrand  $f(\chi)$  of an integral

$$I = \int_{-1}^1 f(\chi) d\chi \quad (\text{A.1})$$

is singular at a certain point  $\chi_0$ , we define the variable in terms of a third-degree polynomial

$$s = \chi_3(t) = at^3 + bt^2 + ct + d. \quad (\text{A.2})$$

And the conditions below are applied to determine the coefficient  $a, b, c$ , and  $d$ . Since  $\chi_3(t): [-1,1] \rightarrow [-1,1]$ ,

$$\chi_3(1) = 1 \quad (\text{A.3a})$$

$$\chi_3(-1) = -1 \quad (\text{A.3b})$$

$$\left. \frac{\partial \chi_3}{\partial t} \right|_{\chi_0} = 0 \quad (\text{A.3c})$$

$$\left. \frac{\partial^2 \chi_3}{\partial t^2} \right|_{\chi_0} = 0 \quad (\text{A.3d})$$

where  $\chi_0 = \chi_3(t_0)$ .

The transformation in general form that satisfies the above conditions is given by [52]

$$\chi_q(t) = \chi_0 + \delta(\chi_0, q)(t - t_0)^q \quad (\text{A.4})$$

where  $q$  is an odd integer. Setting  $\chi_q(1) = 1$  and  $\chi_q(-1) = -1$  gives the unknowns  $\delta(\chi_0, q)$  and  $t_0$  as

$$\delta(\chi_0, q) = 2^{-q} [(1 + \chi_0)^{1/q} + (1 - \chi_0)^{1/q}]^q, \quad (\text{A.5})$$

and

$$t_0 = \frac{(1 + \chi_0)^{1/q} - (1 - \chi_0)^{1/q}}{(1 + \chi_0)^{1/q} + (1 - \chi_0)^{1/q}}. \quad (\text{A.6})$$

By setting  $q = 3$  in the general form of the transformation, we obtain Telles transformation.

# Appendix B

## Two-Dimensional Boundary Integrals

In §5, we compare axisymmetric flow with plane flow by developing two-dimensional boundary integral formulation. The integral equations are derived as in the same analysis in three-dimensional formulation. We apply Lorentz reciprocal relation (3.1) with two-dimensional solutions of (3.2) for velocity and stress fields

$$\mathbf{u}(\mathbf{y}) = \frac{1}{4\pi} \mathbf{G}(\mathbf{x}, \mathbf{y}) \mathbf{b}, \quad (\text{B.1a})$$

$$\boldsymbol{\sigma}(\mathbf{y}) = \frac{1}{4\pi} \mathbf{T}(\mathbf{x}, \mathbf{y}) \mathbf{b}. \quad (\text{B.1b})$$

In two dimensions, the Green's functions are given as

$$G_{ij}(\mathbf{x}, \mathbf{y}) = -\delta_{ij} \ln r + \frac{\widehat{r}_i \widehat{r}_j}{r^2}, \quad (\text{B.2a})$$

$$T_{ij}(\mathbf{x}, \mathbf{y}) = -4 \frac{\widehat{r}_i \widehat{r}_j \widehat{r}_k}{r^4}. \quad (\text{B.2b})$$

The general boundary integral equation for two-dimensional flow is

$$\mathcal{C}(\mathbf{x}) \mathbf{u}(\mathbf{x}) = \frac{1}{4\pi} \int_{\Gamma} \mathbf{G}(\mathbf{x}, \mathbf{y}) \mathbf{f}(\mathbf{y}) dS(\mathbf{y}) - \frac{1}{4\pi} \int_{\Gamma} \mathbf{u}(\mathbf{y}) \mathbf{T}(\mathbf{x}, \mathbf{y}) \mathbf{n}(\mathbf{y}) dS(\mathbf{y}), \quad (\text{B.3})$$

and the boundary integral equation for multiphase flow is

$$\begin{aligned}
\varepsilon \mathbf{C}(\mathbf{x}) \mathbf{u}_\beta(\mathbf{x}) = & -\frac{1}{4\pi} \int_{\Gamma} \mathbf{G}(\mathbf{x}, \mathbf{y}) \mathbf{f}_s(\mathbf{y}) dS(\mathbf{y}) \\
& + \frac{1}{4\pi} \int_{\Gamma} \mathbf{u}_s(\mathbf{y}) \mathbf{T}(\mathbf{x}, \mathbf{y}) \mathbf{n}(\mathbf{y}) dS(\mathbf{y}) \\
& - \frac{1}{4\pi} \frac{1}{Ca} \int_{\Gamma_d} \mathbf{G}(\mathbf{x}, \mathbf{y}) (\nabla \cdot \mathbf{n}(\mathbf{y})) \mathbf{n}(\mathbf{y}) dS(\mathbf{y}) \\
& + \frac{(1-\lambda)}{4\pi} \int_{\Gamma_d} \mathbf{u}_d(\mathbf{y}) \mathbf{T}(\mathbf{x}, \mathbf{y}) \mathbf{n}(\mathbf{y}) dS(\mathbf{y}). \tag{B.4}
\end{aligned}$$

Since the fundamental solutions (B.2) are in two dimensions, we directly integrate them, and the linear system is obtained by summing the integral equations for all elements as below

$$\begin{aligned}
\begin{bmatrix} C_{xx} & C_{xy} \\ C_{yx} & C_{yy} \end{bmatrix}_{ii} \begin{bmatrix} u_x \\ u_y \end{bmatrix}_i = & (1-\lambda) \sum_{j=1}^{N_d} \int_{\Gamma_{d_j}} \begin{bmatrix} T_{xx} & T_{xy} \\ T_{yx} & T_{yy} \end{bmatrix}_{ij} \begin{bmatrix} u_x \\ u_y \end{bmatrix}_j d\Gamma \\
& + \sum_{j=1}^N \int_{\Gamma_j} \begin{bmatrix} T_{xx} & T_{xy} \\ T_{yx} & T_{yy} \end{bmatrix}_{ij} \begin{bmatrix} u_x \\ u_y \end{bmatrix}_j d\Gamma \\
& - \sum_{j=1}^N \int_{\Gamma_j} \begin{bmatrix} G_{xx} & G_{xy} \\ G_{yx} & G_{yy} \end{bmatrix}_{ij} \begin{bmatrix} f_x \\ f_y \end{bmatrix}_j d\Gamma \\
& - \frac{\nabla \cdot \mathbf{n}}{Ca} \sum_{j=1}^{N_d} \int_{\Gamma_{d_j}} \begin{bmatrix} G_{xx} & G_{xy} \\ G_{yx} & G_{yy} \end{bmatrix}_{ij} \begin{bmatrix} n_x \\ n_y \end{bmatrix}_j d\Gamma \tag{B.5}
\end{aligned}$$

In two-dimensional implementation, we use constant elements for the approximation of the coordinates, the velocity, and the traction components. The normal vectors and the surface curvature are calculated by 4<sup>th</sup> order interpolation for better accuracy. The 4<sup>th</sup> order shape functions are

$$\varphi_1(\xi) = (2/3)\xi(\xi - 1)(\xi - 1/2)(\xi + 1/2), \quad (\text{B.6a})$$

$$\varphi_2(\xi) = (8/3)\xi(\xi + 1)(\xi - 1/2)(1 - \xi), \quad (\text{B.6b})$$

$$\varphi_3(\xi) = 4(\xi + 1)(\xi + 1/2)(\xi - 1/2)(\xi - 1), \quad (\text{B.6c})$$

$$\varphi_4(\xi) = (8/3)\xi(\xi + 1)(\xi + 1/2)(1 - \xi), \quad (\text{B.6d})$$

$$\varphi_5(\xi) = (2/3)\xi(\xi + 1)(\xi - 1/2)(\xi + 1/2). \quad (\text{B.6e})$$

# Curriculum Vitae

Name Surname : Büşra Kaya

## Education:

2013–2018 İzmir Kâtip Çelebi University, Dept. of Mechanical Eng.

2018–2022 İzmir Kâtip Çelebi University, Dept. of Mechanical Eng.

## Work Experience:

2021 – present Mitsubishi Electric Turkey Air Conditioning Systems Production Inc., Function Design Responsible

2018 – 2019 İzmir Kâtip Çelebi University Scientific Research Project, Graduate Research Student

## Publications:

1. Kaya B, Ceyhan U. Axisymmetric Deformation of Drops Through Tubes with Asymmetric Constrictions. *Under preparation*.
2. Kaya B, Ceyhan U, Karadeniz ZH. Effect of Cylinders on the Heat Transfer in a Microchannel. 22nd Congress on Thermal Science and Technology 2019.
3. Gungor S, Aydın L, Ceyhan U, Kaya B, Karadeniz ZH. Analysis of Backward and Forward Effects on a Grooved Co-axial Heat Exchanger by Response Surface Methodology. 13th REHVA World Congress CLIMA 2019.